4-21-2010

Surface Plasmon Enhancement of Organic Photovoltaic Devices

Megan Holtz
Trinity University, mholtz@trinity.edu

Surface Plasmon Enhancement of Organic Photovoltaic Devices

Megan Holtz

A departmental honors thesis submitted to the Department of Physics and Astronomy at Trinity University in partial fulfillment of the requirements for graduation with departmental honors.

April 21, 2010

_____	_____
Jennifer Steele	David Hough
Thesis Advisor	Department Chair

_____

Associate Vice President
for
Academic Affairs

Abstract

Organic photovoltaic (OPV) cells have recently attracted attention due to their low cost and easy fabrication. However, their efficiency remains low compared to silicon-based photovoltaics. OPV cells generate power through the creation of an exciton by light. The diffusion length for the electron-hole pair in most organic photovoltaic material is on the order of 100 nm, which limits the overall thickness of the device. The maximum 100 nm thickness of the cell reduces the absorption of the device, which ultimately lowers its efficiency. The absorption may be boosted at certain wavelengths by the excitation of surface plasmons. Surface plasmons are collective oscillations of conduction electrons in the metal along a metal-dielectric interface, and create enhancements of the electromagnetic fields up to 20 times near the metal surface. To test the possible enhancement from surface plasmons, OPV cells are made using a conjugated polymer and fullerene-based active layer with either an aluminum or silver bottom electrode. Periodic grating structures were formed between the active layer and the metal electrode to facilitate surface plasmon excitation from visible light. Surface plasmons are verified to exist on Al cathode cells by reflection and transmission measurements. Although there is no statistically significant change in efficiency, fill factor, open circuit voltage or short circuit current observed for our devices on patterned versus unpatterned OPV cells, this could be due to the large error that results from having small numbers of samples. While there is no overall gain in incident photon conversion efficiency (IPCE) for the samples with gratings to couple surface plasmons, OPV cells with silver cathodes demonstrated gains in IPCE potentially due to surface plasmons around 400 to 450 nm for both 555 nm and 833 nm period gratings. Further experiments are necessary to fully investigate the role of the surface plasmon in this increase in efficiency.

Acknowledgements

I cannot say thank you enough to Dr. Steele for her time, effort and support in advising me on this project and getting the project started. Without her enthusiasm, this project never could have happened. Also, thank you to Dr. MacAlpine for getting me started on renewable energy at Trinity, and finding and letting me borrow "The Big Green Book." It has been so helpful. Dr. Hough, Dr. Spiegel and Dr. Ugolini have been invaluable during the revision process – thank you for your time and comments. Thank you to the Trinity Physics Department for supporting me throughout this project and making this project happen, and for being a wonderful environment in which I could learn and grow. Thanks as well to the department for initially funding me, and to the Mach Foundation for my continued funding – without this there would be no supplies for the project or trips to Austin for fabrication. Also, thank you to Larry for making the metal deposition mask, which makes the OPV cells possible.

Table of Contents

Table of Figures

I. Organic Photovoltaic Cells

Global energy demands are increasing due to growing consumption by industrialized nations and the push to achieve an industrial economy by developing nations. This growing energy consumption makes sustaining the worldwide appetite for energy an escalating problem. As energy demands have grown, carbon-based energy sources have progressed from wood to energy-dense coal, oil, and natural gas. Burning these nonrenewable resources releases the greenhouse gas carbon dioxide, which is linked to global warming.[1] Both escalating energy demands and the ensuing climate crisis are two related problems scientists and engineers must aggressively address. It is vital that renewable energy sources are developed that have a sustainable environmental impact and that are cost compatible with conventional carbon-based energy generation systems.

An area that is critical in advancing our use of renewable energy is the research and development of efficient and inexpensive photovoltaic cells. Sunlight is readily available and solar power generation releases no greenhouse gases. Despite decades of solar cell development, further innovations are needed to improve efficiency and reduce cost. First generation solar cells are comprised of low defect crystalline photovoltaic devices and can achieve an efficiency of 25% for silicon.[2] However, they remain expensive compared to conventional carbon-based energy generation methods. Due to the quality of crystal needed, first generation devices are not expected to produce power cheaper than $1/W, as seen in Figure 1.[3]

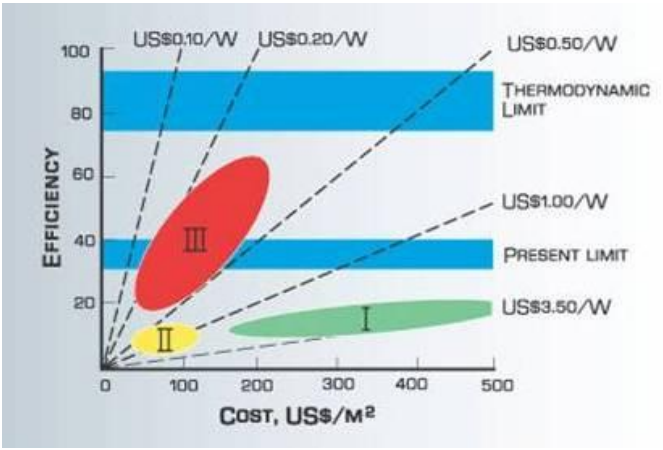

Figure 1: First, second and third generation solar cell efficiency vs. cost. US $/W lines are shown.[2]

Second generation solar cells promise efficiencies and costs approaching $0.50/W. They use thin film technology, which is not as labor or energy intensive to fabricate as crystalline photovoltaic cells. Thin film devices can be flexible and relatively inexpensive. However, efficiencies of these cells are low because of defects caused by lower quality processing methods. One second generation solar cell device that is the basis of this thesis is the organic photovoltaic (OPV) cell; these cells currently have efficiencies around 5%.[2]

Further developments in solar cell technology have led to third generation devices, which achieve higher efficiencies and may reach $0.20/W. Some examples include tandem solar cells, thermoelectric cells, thermophotonic cells, hot carrier cells, and cells that produce more than one electron-hole pair per photon. A 2-terminal multijunction cell (GaInP/GaInAs/Ge) demonstrated a 41.1% efficiency.[2] Recent research in second and third generation solar cells has looked at the use of surface plasmons and nanostructures to further improve efficiency.[4]

A. How Photovoltaic Devices Work

A general schematic of a semiconductor-based solar cell is show in Figure 2. The most general type of semiconductor-based solar cell is the *pn* junction of a silicon solar cell. A *pn* junction is created by fabricating a *p*-type material next to *n*-type material. *p*-type silicon is doped with a group III element, such as boron. Boron doping leaves an extra hole in the crystalline lattice, where an electron would normally reside if the dopant were not there. The hole in the lattice effectively creates an energy state just above the valence band energy. *n*-type silicon is doped with a group V element such as phosphorous. This introduces an extra electron into the lattice, effectively creating an energy state just below the conduction band.[5]

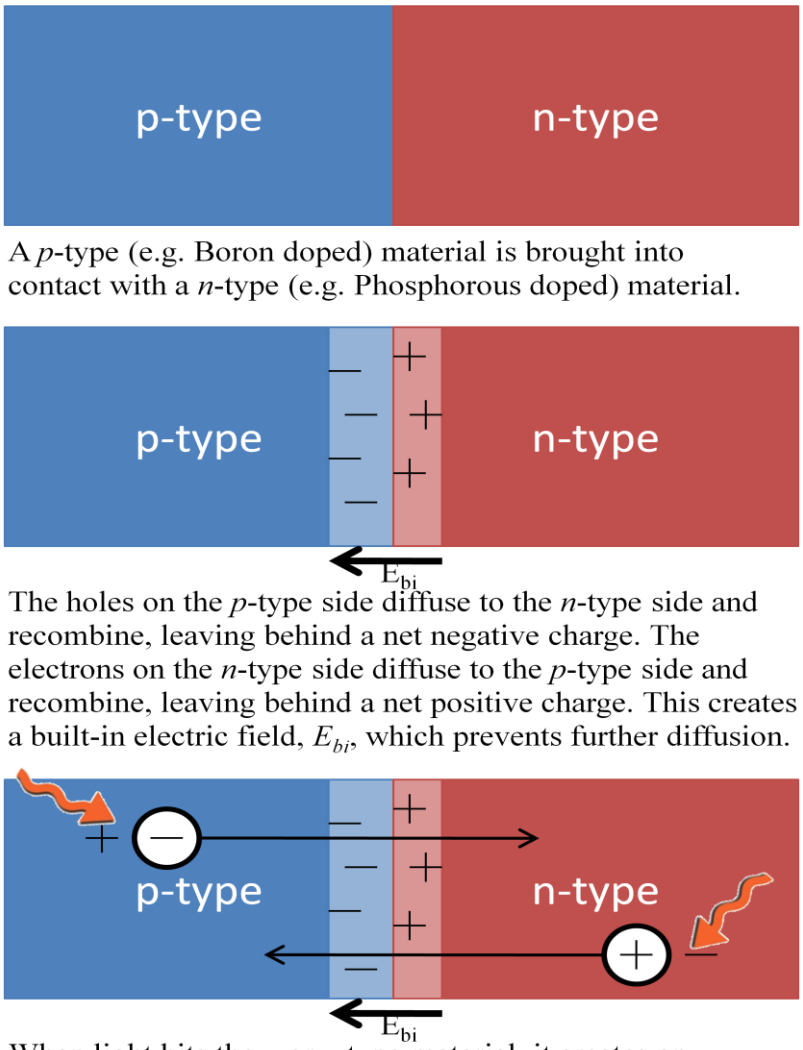

Figure 2: Annotated schematic of a *pn* junction solar cell.

When the two materials are in contact with each other, the holes in the *p*-type silicon diffuse to the *n*-type side and recombine with the extra electron in the *n*-type material, leaving behind a net negative charge on the *p*-type side. The electrons in the *n*-type silicon diffuse to the *p*-type and recombine with the extra holes in the *p*-type material, leaving a behind net positive charge on the *n*-type side. The area in which there is a net charge on the solar cell is called the depletion layer. Across the depletion layer is a built-in electric field, E_{bi}, caused by the buildup of charge. When at equilibrium, E_{bi} prevents further charge diffusion.

When light is absorbed by the solar cell, an electron is excited from the valence band to the conduction band. This creates an electron-hole pair. On the *p*-type side, the built-in electric field, i.e. the electric field created by the charge build-up in the depletion region, sweeps the electron to the n-type side where it can be collected at the electrode, but the hole is trapped on the *p*-type side. On the *n*-type side, the situation is reversed. The hole is swept to the *p*-type side but the electron is trapped on the *n*-type side. The holes are collected at the anode and the electrons are collected at the cathode. When there is a load across the photovoltaic cell, a current flows and power is generated.

While the *pn* junction solar cell is a beautiful example of condensed matter theory at work, the functioning of OPV cells relies heavily on chemistry. OPV cells work in a similar way to silicon-based solar cells in the sense that when light hits the device, an electron-hole pair is generated and current is swept in a particular direction to generate power. However, there are fundamental differences about how the electron-hole pair is generated, how the charge is transported, and what creates the potential difference in the various types of OPV cells.

OPV cells are generally classified by the materials that comprise the cell, such as polymers, fullerenes, and dyes. OPV cells are also classified by their structure - for example,

bulk heterojunction, layered heterojunction, homojunction, liquid crystal, and nanostructured. Most OPV cells consist of a cathode, active layer, and anode. The active layer generates current when illuminated with light. Analogous to the *n*-type and *p*-type doping for silicon-based solar cells, OPV cells have an active layer comprised of a donor material, which gives up electrons, and an acceptor material, which gives up holes (or accepts electrons). If the donor and acceptor materials are distinct chemicals, the cell is said to have a heterojunction active layer. The active layer is classified as a bulk heterojunction if the acceptor and donor materials are in solution together when deposited, forming an amorphous layer. The other common type of heterojunction solar cell has a bilayer, where the acceptor material is deposited on top of the donor material. We will focus on the bulk heterojunction solar cell comprised of the conjugated polymer poly(3-hexylthiophene) (P3HT) and the fullerene 1-(3-methoxycarbonyl)-propyl-1-phenyl-(6, 6)C_{60} (PCBM) in a chlorobenzene solution, with aluminum or silver and indium tin oxide (ITO) electrodes.

Before we can discuss how our particular OPV works, we must first take a look at the chemicals comprising our active layer. For our OPV cells, the conjugated polymer P3HT acts as the donor and the fullerene PCBM acts as the acceptor. P3HT and PCBM are shown in Figure 3 (a)[6] and (b)[7] respectively. Their energy band diagrams are shown in Figure 4.[8]

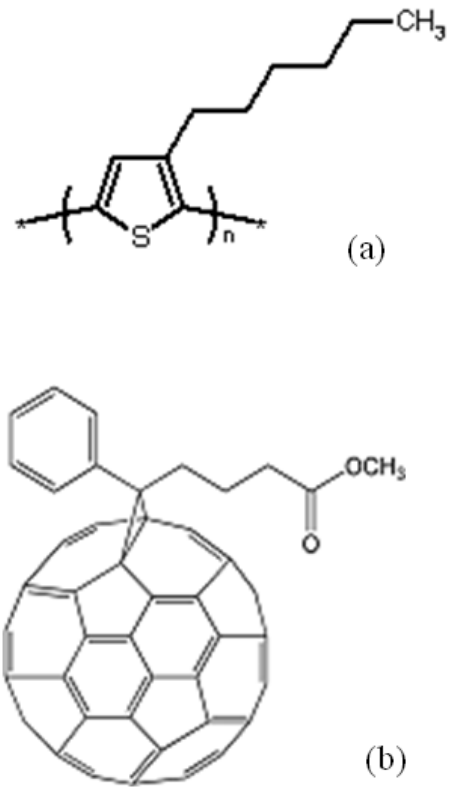

Figure 3: Chemical structure of P3HT (a) and PCBM (b).

Conjugated polymers are commonly used in OPV cells due to the structure of the polymer. A conjugated polymer is a chain of alternating single and double covalent bonds between carbon atoms. The effect of the alternating single and double bonds is that there are delocalized electrons in the polymer, which are not bound to one particular atom but rather the entire chain of atoms. Such electrons are said to be the delocalized π electrons, and are free to move about the polymer chain. Because the delocalized electron is not strongly bonded to the polymer, it is in the highest occupied molecular orbital (HOMO) and is the electron that is most easily excited to the lowest unoccupied molecular orbital (LUMO).

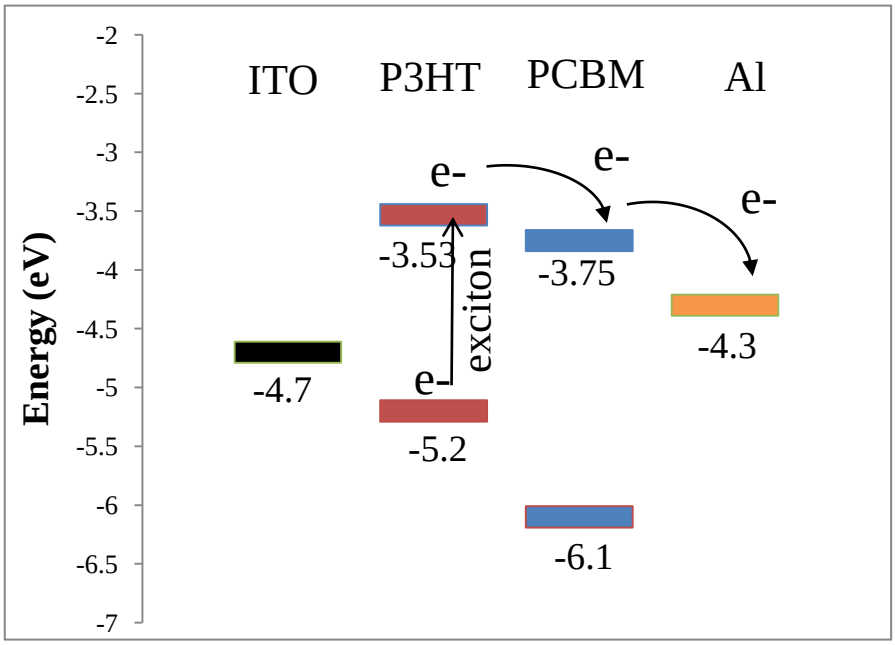

Figure 4: Work functions of the two electrodes (ITO and Al) and the HOMO and LUMO levels of P3HT, PCBM, with vacuum at 0 eV.

One of the main differences between how OPV cells work and how-semiconductor based solar cells work is that when light strikes the cell, OPV cells form excitons while semiconductors form electron-hole pairs.[9,10] An exciton is an excited electron and hole pair that is electrically neutral and is bound by Coulomb attraction in a nonmetal material. Usually the exciton is formed from energy from an incident photon. Physically, the excitons occur because there is a large Coulomb force between the excited electron and its nucleus in the OPV donor material. An electron will become "free" from its Coulomb attraction to its nucleus if the energy of attraction

is less than the average thermal energy of the carrier. The threshold at which an electron becomes free occurs at an energy where[6]

$$\frac{e^2}{4\pi\kappa\varepsilon_o r_c} = k_B T \qquad \text{[Eq. 1]}$$

where e is the charge of the electron, κ is the dielectric constant, ε_o is the permittivity of free space, r_c is the critical distance between the two charges, k_B is the Boltzmann constant, and T is the temperature. If the Bohr radius of the atom, which is the root mean square radius of an atom from the center of the nucleus to the outer electron waveform, is smaller than the critical radius, an exciton will be formed. If the Bohr radius is larger than the critical radius, an electron-hole pair will be formed. The Bohr radius for electrons in a solid is defined as

$$r_B = n^2 a_o \kappa \frac{m_e}{m_{eff}} \qquad \text{[Eq. 2]}$$

where a_o is the Bohr radius of hydrogen, n is the principal quantum number, m_e is the mass of the free electron in vacuum and m_{eff} is the effective mass of the electron in the semiconductor or organic material. The Bohr radius in OPV cells is much smaller than in semiconductor cells, because κ is lower and m_{eff} is larger.

We can define γ as:

$$\gamma = \frac{r_c}{r_B} = \left(\frac{e^2}{4\pi\varepsilon_o k_B n^2 a_o m_e}\right)\left(\frac{m_{eff}}{\kappa^2 T}\right) \qquad \text{[Eq. 3]}$$

When $\gamma > 1$, $r_c > r_B$ and excitonic behavior is seen. In general, $\gamma >> 1$ for OPV cells. When $\gamma < 1$, $r_c < r_B$ and electron-hole pairs are produced. Semiconductor-based solar cells have $\gamma < 1$.[9]

When light strikes a semiconductor-based solar cell, the electrons and holes are separated instantaneously and are free from electrostatic interaction with each other. However, in OPV devices, electrically neutral excitons are formed. The excitons must be separated into electron-hole pairs some other way, and this happens at the heterojunction interface. The process of

splitting the electron and hole can be seen on a potential energy level diagram, Figure 4. The delocalized π electron in P3HT absorbs the energy of an incoming photon and is excited from the HOMO energy level to the LUMO energy level in the P3HT polymer. Once it reaches this excited state, it is "donated" to the PCBM molecule which has a lower energy LUMO. Once the electron is accepted by the PCBM, it can be transported from one PCBM molecule to another. This charge transfer state has a long lifetime, implying a high quantum efficiency if the electron is successfully donated to the PCBM. The high lifetime of the state allows the electron to be moved throughout the active layer.

Since the active layer is uniform, the transport of the electron between PCBM molecules will be random unless the symmetry of the device is broken. Direction is given to the charge transport by giving the anode and the cathode different work functions, which generate a built-in electric field. The work function is the minimum energy needed to remove an electron from a material. The anode is designed to have a lower work function than the cathode, so electrons will be transported towards the anode and holes will be transported towards the cathode. This can be seen in Figure 5. The Fermi levels of the metals are shown, which is related to their work function. Since we have taken the vacuum to be at zero energy, the Fermi energy has the same

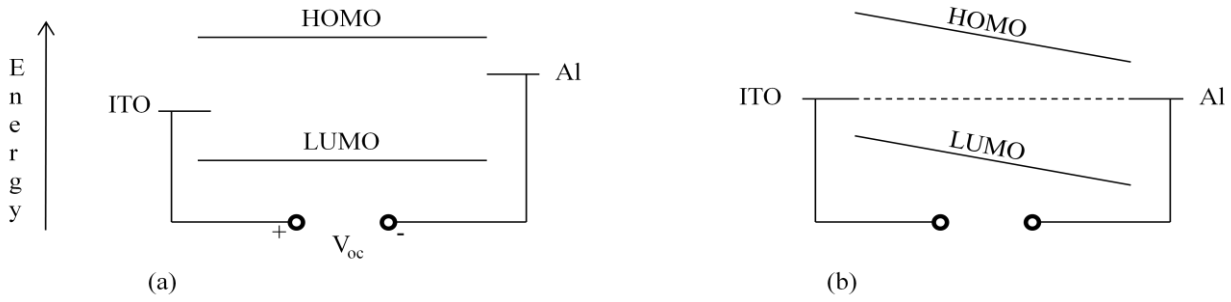

Figure 5: Metal-insulator-metal picture for an organic solar cell in (a) open circuit condition and (b) short circuit condition.

magnitude as the work function. The organic materials are represented on the diagram by their HOMO and LUMO levels. For open circuit conditions (Figure 5 (a)), we see the open circuit voltage across the terminals. Because in open circuit conditions no current is able to flow, the open circuit voltage must match the difference in the work functions of the two electrodes. When the OPV is short circuited (Figure 5(b)), i.e. there is no applied voltage, the Fermi levels of the two metals must match and the HOMO and LUMO energy lines shift accordingly. In the dark, no current flows for this device, but under illumination the built-in electric field created by the difference in work functions will drive holes to the anode and electrons to the cathode.

The choice of anode for many OPV bulk heterojunction cells is a thin layer of poly(3,4-ethylenedioxythiophene): poly(styrenesulfonate) (PEDOT-PSS) on top of ITO coated glass. The PEDOT-PSS is an organic conductor that provides a high work function and smoothes the physical interface between the ITO and the active layer.[11] A higher work function cathode, such as Al or Ag, is used to collect the electrons.

B. Electrical Characteristics of OPV Cells

In order to quantify the efficiency of the OPV cells, some key device characteristics must be understood. Electrical characteristics that define the efficiency of the cell include the overall efficiency (η), the fill factor (FF), open circuit voltage (V_{oc}), short circuit current (I_{sc}), and the incident photon conversion efficiency (IPCE). Note that some authors refer to the external quantum efficiency (EQE) instead of the IPCE, but the two terms are equivalent.

The overall efficiency is defined as the ratio of the power output from the solar cell to the power input from the incident light:

$$\eta = \frac{P_{cell}}{P_{light}} = \frac{V_{mp}\, I_{mp}}{GA} \qquad \text{[Eq. 4]}$$

where G is the irradiance of the incident light in W/m^2, A is the area of the cell, and V_{mp} and I_{mp} are the voltage and current given by the solar cell at maximum power output.

The fill factor is described by the maximum power point for a given photovoltaic cell with a certain V_{oc} and I_{sc}: [12]

$$FF = \frac{V_{mp}\, I_{mp}}{V_{oc}\, I_{sc}} \qquad \text{[Eq. 5]}$$

A typical I-V curve showing the fill factor, open circuit voltage, and short circuit current are shown in Figure 6. The fill factor can be seen graphically as the ratio of the dark shaded region to the light shaded region. The fill factor is related to the overall efficiency by

$$\boldsymbol{\eta = \frac{(FF)V_{oc}I_{sc}}{GA}} \qquad \text{[Eq. 6]}$$

We can rearrange to find that the fill factor is

$$\boldsymbol{FF = \frac{\eta GA}{V_{oc}I_{sc}}} \qquad \text{[Eq. 7]}$$

The IPCE, also referred to as the external quantum efficiency, is given by [12]

$$IPCE = EQE = \frac{n_e}{n_{ph}} = \frac{I_{sc}}{G_\lambda A}\frac{hc}{\lambda e} \qquad \text{[Eq. 8]}$$

where n_e is the number of electrons produced, n_{ph} is the number of incident photons, h is Planck's constant, c is the speed of light, λ is the wavelength of light, G_λ is the irradiance at the wavelength λ and e is the charge of the electron. The IPCE is important in

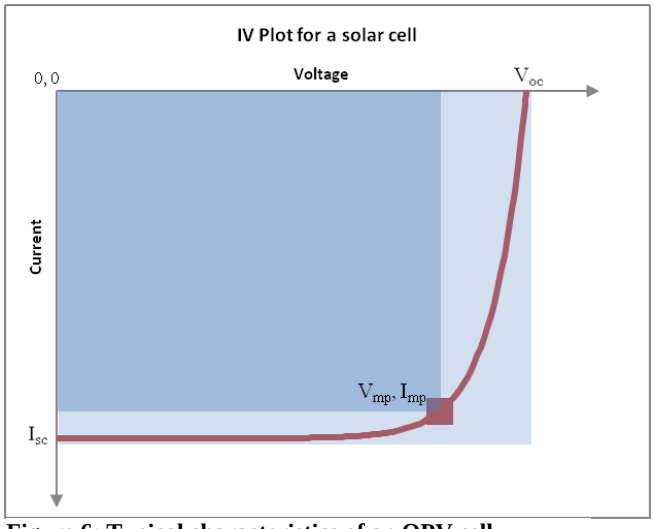

Figure 6: Typical characteristics of an OPV cell.

understanding the efficiency of the cell at different wavelengths. Because the IPCE depends on the total number of photons incident on the cell, the IPCE is proportional to the absorption of the active layer material. If absorption is boosted, the IPCE will be higher.

C. Structure and Limitations of OPV Cells

There are several limitations on how OPV cells can be designed. One limitation of OPV cells is that the diffusion length of the primary photoexciton is small, on the order of 10 nm. This means that donor and acceptor molecules must be within 10 nm for efficient charge generation. One characteristic of an amorphous bulk heterojunction layer is that there is a large interfacial area between the donor and acceptor materials, allowing for the electron to be collected by the acceptor molecule. We would like the bulk heterojunction solution to be as uniform and well distributed as possible. The solvent chlorobenzene has been shown to dissolve the acceptor and donor atoms such that cast films have high smoothness and no large-scale features that can be seen using an AFM.[12]

Another limitation that is not as simple to solve is the poor charge carrier mobility, which strictly limits the short circuit photocurrent. Since the electrons need to be able to travel from one side of the device to the other, the thickness of the active layer is restricted to the mean free path of the electrons (~100 nm for amorphous organic materials).[13] This restricts the active layer thickness to 100 nm. Because the active layer is so thin, absorbing light is especially difficult, as much of the light incident on the cell is reflected or transmitted. Even though most polymers have strong optical absorption coefficients, further improvements in the absorption efficiency of the cell could greatly enhance overall efficiency. Many different methods have been used to improve the absorption efficiency. One widely used method is to increase the optical path length

of the light in the active layer. This can be done by roughing the surface, creating internal reflection in the active layer.[14-16] Another way in which light could be absorbed is by exciting surface plasmons on the metal-dielectric interface between cathode and active layer.[17]

II. Surface Plasmons

An idea for research to increase the absorption efficiency of OPV cells is to use surface plasmons (SPs). SPs are electromagnetic surface waves that exist at a metal-dielectric interface, and are excited by light or electrons. At resonance, the incoming light is transformed into SPs, reducing the reflected beam off the interface, and essentially increasing the absorbance. The basic theory behind SPs can be seen most simply on a smooth metal-dielectric interface.[18] The conduction electrons in the metal boundary can form coherent longitudinal charge oscillations making surface plasmon waves. If we take the *x* direction to be in the direction parallel to the boundary and *z* to be perpendicular the the surface, as in Figure 7, the electric and the magnetic fields are described by:[18]

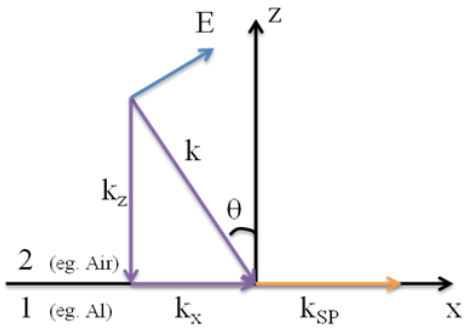

Figure 7: Surface plasmon geometry.

$$\boldsymbol{E}_i = \begin{pmatrix} E_{xi} \\ 0 \\ E_{zi} \end{pmatrix} \exp[+j(k_{xi}x \pm k_{zi}z - \omega t)] \qquad \text{[Eq. 9]}$$

$$\boldsymbol{H}_i = \begin{pmatrix} 0 \\ H_{yi} \\ 0 \end{pmatrix} \exp[+j(k_{xi}x \pm k_{zi}z - \omega t)] \qquad \text{[Eq. 10]}$$

where $j = \sqrt{-1}$, $z \leq 0$ corresponds to region i=1 and (-) and $z \geq 0$ corresponds to region i=2 and (+). The continuity equations state that at $z = 0$:

$$E_{x1} = E_{x2} \qquad \text{[Eq. 11]}$$

$$H_{y1} = H_{y2} \qquad \text{[Eq. 12]}$$

$$\varepsilon_1 E_{z1} = \varepsilon_2 E_{z2} \qquad \text{[Eq. 13]}$$

From the first two continuity equations, we see that

$$k_{x1} = k_{x2} \equiv k_x \quad \text{[Eq. 14]}$$

We can find a relation for k_z by solving Ampere's law (in Gaussian units):

$$\boldsymbol{\nabla} \times \boldsymbol{H}_i = \frac{\varepsilon_i}{c}\frac{\partial}{\partial t}\boldsymbol{E}_i \quad \text{[Eq. 15]}$$

where ε_i is the dielectric constant of region i and c is the speed of light. To find k_z we can isolate the x component of the curl for regions 1 and 2:

$$k_{z1}H_{y1} = -\frac{\omega}{c}\varepsilon_1 E_{x1} \quad \text{[Eq. 16]}$$

$$k_{z2}H_{y2} = \frac{\omega}{c}\varepsilon_2 E_{x2} \quad \text{[Eq. 17]}$$

and the z component, which we will need later, is

$$k_{xi}H_{yi} = -\frac{\omega}{c}\varepsilon_i E_{zi} \quad \text{[Eq. 18]}$$

From Eq. 11 and Eq. 12, we can rearrange the x component to find that

$$\frac{k_{z1}}{\varepsilon_1} + \frac{k_{z2}}{\varepsilon_2} = 0 \quad \text{[Eq. 19]}$$

Similarly, we can solve Faraday's law to relate k_x and k_{zi}.

$$\boldsymbol{\nabla} \times \boldsymbol{E}_i = -\frac{1}{c}\frac{\partial}{\partial t}\boldsymbol{H}_i \quad \text{[Eq. 20]}$$

The y component gives us the interesting solutions this time:

$$k_{z1}E_{x1} + k_x E_{z1} = -\frac{\omega}{c}H_{y1} \quad \text{[Eq. 21]}$$

$$k_{z2}E_{x2} - k_x E_{z2} = -\frac{\omega}{c}H_{y2} \quad \text{[Eq. 22]}$$

Using our solutions from Ampere's law above, we can substitute to find

$$k_x^2 + k_{zi}^2 = \varepsilon_i\left(\frac{\omega}{c}\right)^2 \quad \text{[Eq. 23]}$$

and combining our two results (Eq. 19 and Eq. 23) we can solve to get the dispersion relation:

$$k_x = \frac{\omega}{c}\left(\frac{\varepsilon_1\varepsilon_2}{\varepsilon_1+\varepsilon_2}\right)^{1/2} \quad \text{[Eq. 24]}$$

We assume a real ω. Since region 2 is a dielectric (e.g. air), ε_2 is real. The dielectric constant of the metal in region 1 is $\varepsilon_1 = \varepsilon_1' + i\varepsilon_1''$. We also assume that $\varepsilon_2 < |\varepsilon_1'|$, as this is the case for metals. From these assumptions, we can write k_x with real and imaginary parts, $k_x = k_x' + ik_x''$, where

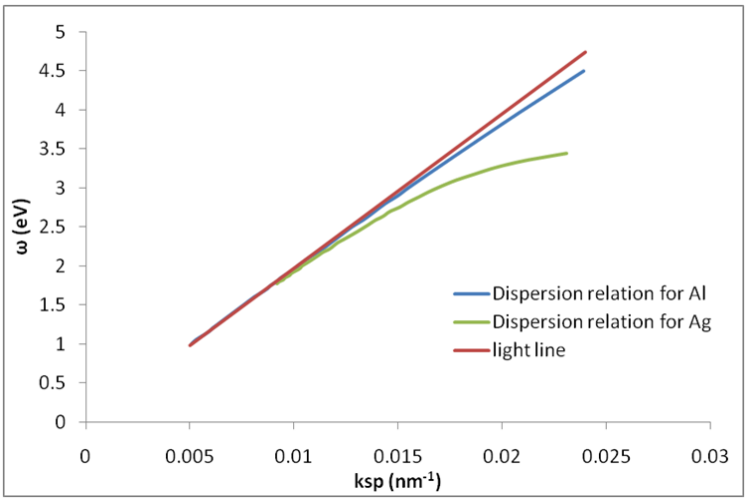

Figure 8: Dispersion curve for Ag and Al plotted with the light line.

$$k_x' = \frac{\omega}{c}\left(\frac{\varepsilon_1'\varepsilon_2}{\varepsilon_1'+\varepsilon_2}\right)^{1/2} \quad \text{[Eq. 25]}$$

$$k_x'' = \frac{\omega}{c}\left(\frac{\varepsilon_1'\varepsilon_2}{\varepsilon_1'+\varepsilon_2}\right)^{3/2}\frac{\varepsilon_1''}{2(\varepsilon_1')^2} \quad \text{[Eq. 26]}$$

Note that ε_1' must be negative and have a larger magnitude than ε_2 for k_x' to be real. For extremely large k_x, the value of ω is no longer linear in k_x but approaches

$$\omega_{SP} = \left(\frac{\omega_p}{1+\varepsilon_2}\right)^{1/2} \quad \text{[Eq. 27]}$$

where ω_p is the plasma frequency $\sqrt{4\pi ne^2/m}$ in Gaussian units, where n is the bulk electron density.

In the case of surface plasmons being excited by light, the dispersion relation for the surface plasmon exists to the right of the light line as shown in Figure 8. The light line is the relation $k = \omega/c$, which has the x component:

$$k_x = \frac{\omega}{c}\sin(\theta) \quad \text{[Eq. 28]}$$

where θ is the incidence angle of the light. In order for there to be interaction between the light and the surface plasmon, there must be a (k_x, ω) pair that satisfies both the incoming light and the SP dispersion relation, i.e. the light line and the surface plasmon dispersion curve must cross. The light line and the dispersion curve for a silver/air boundary and an aluminum/air boundary is plotted in Figure 8; the frequency-dependent dielectric constant for silver was obtained from Johnson and Christy[19] and the frequency-dependent dielectric function for aluminum was obtained from Smith.[20] We can see graphically that the photon wavevector must be increased by Δk_x to see any photon-surface plasmon coupling. This can be achieved by using a grating on the metal-dielectric interface. When light strikes a grating with a period a at an angle θ, the x component of the wave number consists of the x component of the light line plus a Δk_x that stems from the periodicity of the grating, $G = 2\pi/a$:

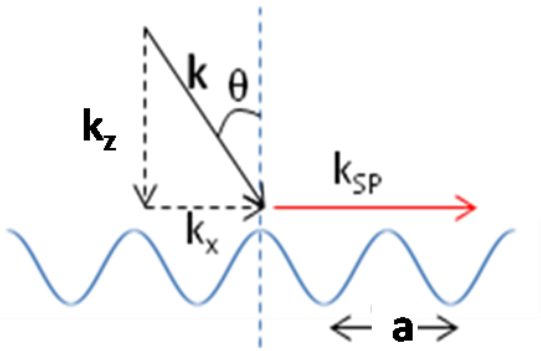

Figure 9: For SPs, k_{SP} depends on k_x and the grating period a.

$$k_x = \frac{\omega}{c}\sin(\theta) + \Delta k_x = \frac{\omega}{c}\sin(\theta) + mG \qquad \text{[Eq. 29]}$$

where m is an integer. The diagram of the wavenumbers on a grating is shown in Figure 9.[18] In order for this wavenumber to couple to a surface plasmon the SP dispersion curve must be satisfied:

$$k_x = \frac{\omega}{c}\sin(\theta) + mG = \frac{\omega}{c}\left(\frac{\varepsilon_1\varepsilon_2}{\varepsilon_1+\varepsilon_2}\right)^{1/2} = k_{SP} \qquad \text{[Eq. 30]}$$

For this to be true, m $\neq$ 0 because that would imply $\Delta k_x = 0$, and there will be no solution to the dispersion equation. Light lines corresponding to m = 0 and ±1 with an incidence angle of 30°

are shown on Figure 10. The effect of the grating period is to allow free space photons to increase their wavevector along the surface of the grating by +/- *mG*, allowing for coupling between free space light and surface plasmon waves.

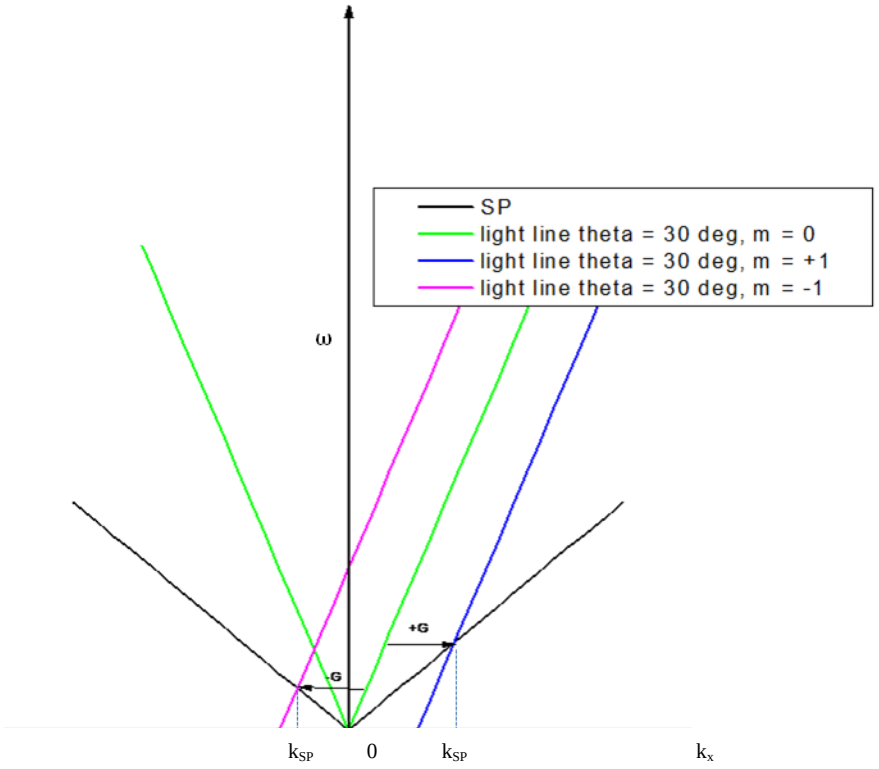

Figure 10: The SP dispersion curve, the light line at 30 deg incidence, and the m = +/- 1 orders for light coupled using a grating.

Because SPs exist in the interface of the metal and dielectric, the boundary conditions between the two materials determine how they propagate and at what resonance frequency they will be most strongly excited. A highly controlled boundary, such as a grating, is an ideal interface to promote particular surface plasmon resonances. The SP resonance can be tuned by changing either the grating period or the angle of incidence of the light, as seen in Eq. 30. Because the light at the SP resonance is the most strongly absorbed, we can select a specific wavelength that we want to be most strongly absorbed in the material.

This has promising applications in photovoltaic devices. SPs demonstrate strong absorption and have been shown to boost absorption efficiency.[16] A boost of absorption of light around 550 nm is expected to offer the best optimization of the efficiency because it enhances the strongest range of the solar irradiance spectrum. However, the optimal SP resonance may be in regions of the solar spectrum where the efficiency of the active layer is weaker. If the ideal frequency for SP resonance is found for this type of OPV, gratings can be manufactured to make an OPV cell with an ideal SP resonance for light perpendicular to the surface. If a strong gain in efficiency is found for a certain grating period, studying SP resonances in various types of OPV cells is warranted.

Another potential benefit of adding gratings to OPV cells is that the surface plasmons would aid in collecting light at different incidence angles that occur from sunrise to sunset. In many silicon-based solar panels, the panels must be rotated in order to have the highest efficiency at normal incidence throughout the day. For surface plasmons excited using gratings, different angles of incident light and different orders ($m = 1, 2, 3\ldots$) would enhance absorption at various wavelengths throughout the day. The tunability afforded by gratings makes them an attractive plasmonic system for the enhancement of OPV cells.

III. Experimental Methods

A. OPV Fabrication Overview

The simplified OPV cell design we used is shown in Figure 11(a), with designs that we fabricated shown in (b, c). The cathode is the transparent conductor (ITO) with 10 Ω/sq resistivity on a 1" by 1" glass substrate. Next, a 20 nm thick layer of filtered PEDOT-PSS is spin coated onto the ITO. Then, an 80 nm thick active layer is spin coated onto the PEDOT-PSS. The active layer consists of P3HT and PCBM in a chlorobenzene solution. To form the grating structure on the active layer, a poly(dimethylsiloxane) (PDMS) mold is formed from a commercially purchased diffraction grating. If a grating is desired between the active layer and cathode, the mold is brought into contact with the uncured P3HT – PCBM active layer and annealed on a hot plate. After annealing, the mold is removed and the aluminum or silver anode is deposited in a thermal evaporator. This general procedure is taken from Ref. 14.

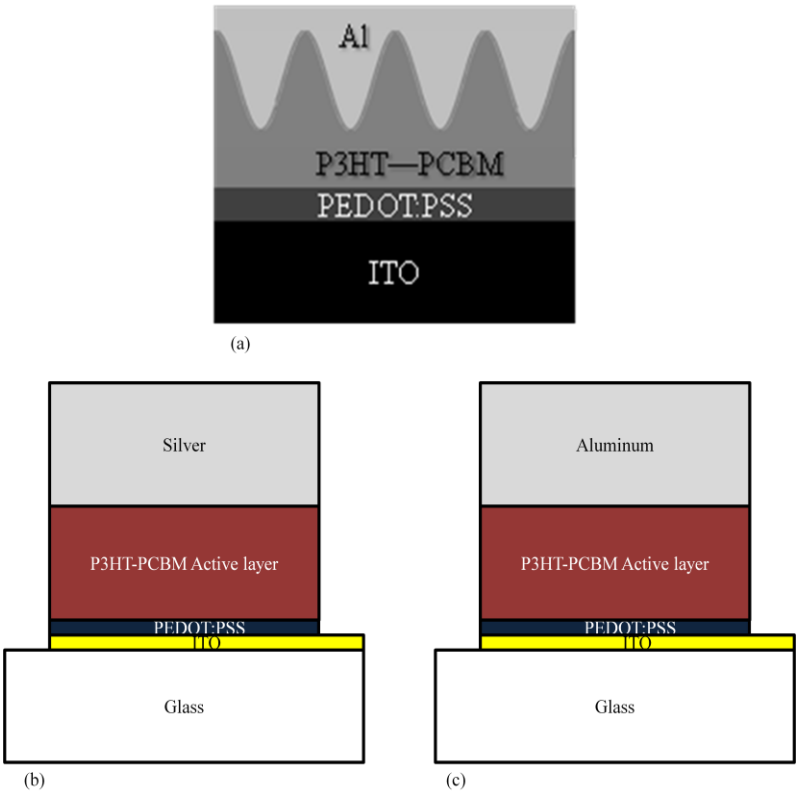

Figure 11: General schematic of the OPV cell.

i. ITO and Chemical Preparation

The ITO is first cleaned by sonication in ethanol and rinsed with deionized (DI) water. Then, the conducting ITO layer is etched away on one edge of the sample with 17 % HCl for one hour to ensure no conductivity. The etchant is rinsed away carefully and thoroughly and the ITO is then cleaned again by sonicating in 60° C DI water and glass detergent for 10 minutes, DI water for 10 minutes, ethanol for 5 minutes and acetone for 5 minutes. The slides are rinsed with DI water after each solution. After the final sonication and rinse, the slides are dried with nitrogen and then heated to 110° C on a hot plate for two minutes to ensure that they are completely dry.

The active layer is composed of P3HT and PCBM in a chlorobenzene solution. To prepare the active layer, a solution of 300 mg P3HT in 10 mL chlorobenzene and a solution of 240 mg PCBM in 10 mL chlorobenzene are stirred separately for 12 hours at room temperature. After 12 hours, the two solutions are mixed and stirred for another 12 hours.[21] The PEDOT-PSS is filtered using a 0.45 micron PDVF filter as instructed by Clevios.[22]

ii. Making PDMS Molds

The PDMS molds are prepared by mixing 10% by weight elastomer curing agent with silicone elastomer base. Typically 25 to 30 g of base is measured in a large petri dish bottom. The curing agent is quickly and evenly pipetted into the petri dish, and mixed vigorously until white with bubbles. The mixture is then placed under vacuum for ~10 minutes until all bubbles have been removed. The master gratings, which consist of 555 nm and 833 nm period diffraction gratings with sine wave profiles, are placed on top of the PDMS quickly and carefully to avoid trapping air under the grating. The PDMS is baked for an hour at 70° C. The PDMS is

removed from the dish and the grating direction is marked on the bottom of the grating. A razor is used to cut the PDMS molds out of the gel and then in half (yielding ~1 cm^2 squares).

iii. OPV Fabrication

While spin coating the PEDOT-PSS and active layer, tape is used to protect the glass slide where the ITO was etched away for the cathode contact area and on the opposite edge for the anode contact area. Then the PEDOT-PSS is spin coated onto the ITO. For a film thickness of 20 nm, we spin coat at 1250 rpm for 30 seconds. The PEDOT-PSS is then annealed on a hot plate at 110° C for 5 minutes in a nitrogen atmosphere to thoroughly remove the water from the PEDOT-PSS layer.

The active layer is deposited on top of the PEDOT-PSS layer. In order to achieve an 80 – 100 nm thick active layer, we spin coat the P3HT-PCBM solution at 1000 rpm for 30 seconds. If a grating is desired, the PDMS mold is immediately placed on top of the active layer. The PDMS mold is tapped very lightly to ensure good contact between the mold and the active layer. The OPV is placed on a hot plate at 110° C in a nitrogen atmosphere for 20 minutes.

The PDMS mold is then removed and the OPV is placed in a thermal or electron beam evaporator. 125 nm of Ag or Al, corresponding to Figure 11 (b) and (c), are evaporated on top of the sample through a mask which determines the area of the OPV – for us, 0.11 cm^2. When the sample is removed, dots of silver paint are placed on the cathode and anode contacts to provide better grips for measuring the electrical properties of the OPV. Silver and aluminum are compatible and interchangeable electrically because their work functions are so similar (4.26 eV and 4.28 eV respectively).[23] While Al is commonly used in OPV cells, Ag has been extensively studied in plasmonics.[24]

B. Surface Plasmon Resonance Measurements

Reflection measurements are made to locate the surface plasmon resonance. The set-up is shown in Figure 12. Light from a white light source is polarized so that the incident electric field is parallel to the plane of the surface of the sample and perpendicular to the lines of the grating at normal incidence, exciting surface plasmons in the sample. The light is collimated and filtered by a medium density filter before going through an iris diaphragm. A spot of light hits the sample, which is on a rotating stand. The sample and the collector are rotated to measure the reflected light at different angles of incidence. The light is transmitted through a fiber optic cable to a spectrometer, which contains a charge-coupled device (CCD) array which measures the intensity of the reflected light as a function of wavelength. The spectrometer readings are sent to a computer, where the data can be recorded and analyzed by SpectraSuite (Ocean Optics).

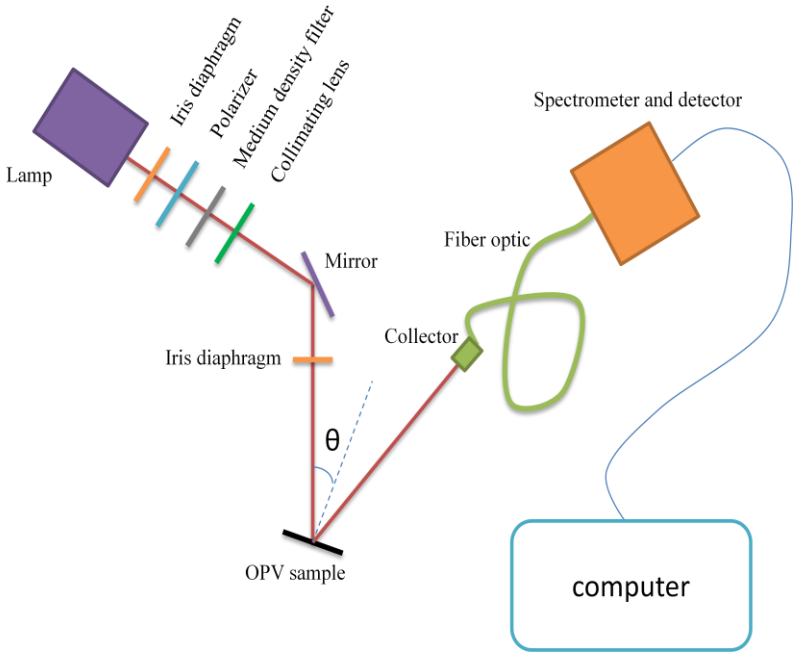

Figure 12: Reflection data set up.

C. Electrical Characterization

The I-V curves of the solar cells are determined by an AM 1.5 lamp which is calibrated using a Si photodiode to be within 1% of the National Renewable Energy Laboratory (NREL)

standards. I-V curves are measured first for both the OPV in the dark and under illumination. I-V curves are measured in three regions: the negative voltage region where the OPV is reverse biased, through the power generating region ($0 \leq V \leq V_{oc}$), and $V \geq V_{oc}$. To measure all three voltage ranges, an external voltage is applied to the OPV device and the current is measured. From the I-V curve, the open circuit voltage, the short circuit current, fill factor and total efficiency of the cell can be measured given a known light source.

The IPCE is measured by shining single-wavelength light produced by a monochromator on the OPV and measuring the resulting current. The angle of the incident light is changed using a rotating stand. Both the I-V curves and the IPCE measurements are done using an Angstrom Engineering system at the Center for Nano and Molecular Science and Technology at the University of Texas at Austin.

IV. Results and Discussion

A. Surface Plasmon Measurements

Surface plasmon resonance was measured by reflection and transmission for OPV cells made on March 10, 2010. These OPV cells are fabricated as above, but only have 40 nm thick Al electrodes. Reflection data were taken from θ = 3° up to 20°, with data sets taken for the incident beam striking either the active layer side or air side of the Al film. Figure 13 shows the air side reflection for a 555 nm and an 833 nm patterned sample, and Figure 14 shows the active layer side reflection for a 555 nm patterned sample. The reflection spectra of the patterned OPV cells are normalized to the reflection spectra of the blank OPV cells at each incidence angle.

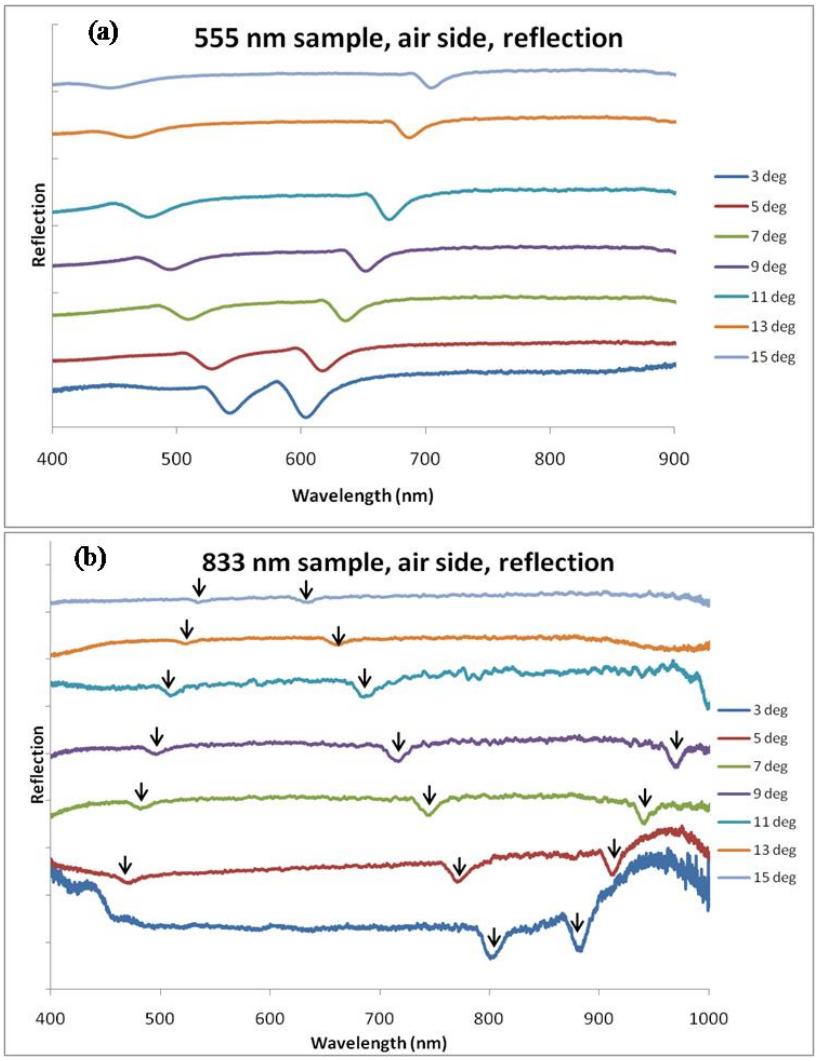

Figure 13: OPV reflection data on an air/Al boundary for (a) a 555 nm patterned sample, and (b) an 833 nm patterned sample.

The surface plasmon resonance is seen in Figure 13 and in Figure 14 as dips in the reflection, where more light is being absorbed by the excitation of a surface plasmon. In graphs

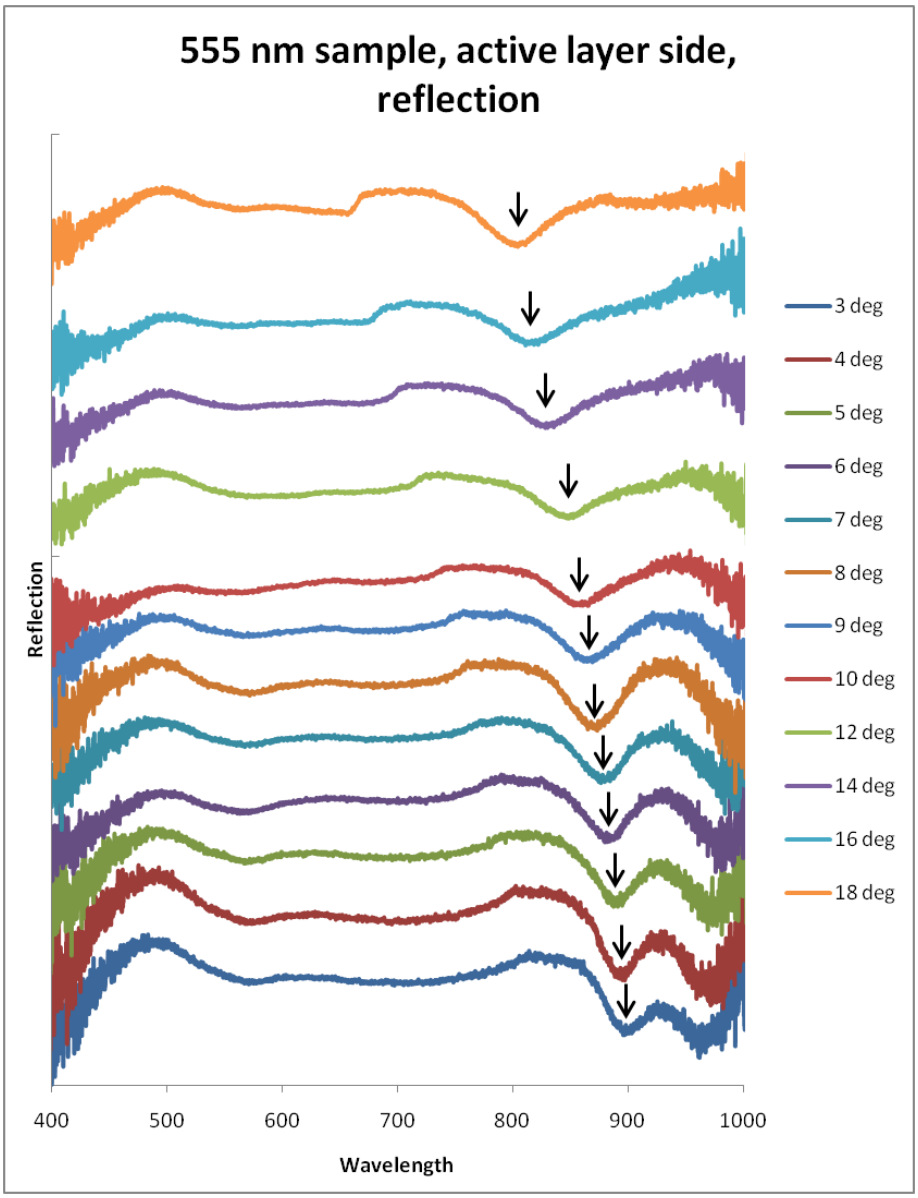

Figure 14: OPV reflection data on an active layer/Al boundary for a 555 nm patterned sample.

in which the surface plasmon is not always readily visible due to scaling, arrows indicate where the surface plasmons reside. We see the surface plasmons on the aluminum-air interface for OPV cells with both 555 nm gratings and 833 nm gratings. On the aluminum-active layer interface we see surface plasmons for the 555 nm gratings. Active layer side reflection spectra of the 833 nm patterned devices are omitted from Figure 14 because no surface plasmon activity was seen.

For the data sets in Figure 13 and Figure 14, reduced zone dispersion curves were generated in Figure 15 (a-c) using Eq. 28 and finding omega in eV. The convention for the dispersion curve plot is to graph omega $= \hbar\omega = hc/\lambda_{SP}$, where λ_{SP} is the wavelength where the surface plasmon occurs. We see that surface plasmons are excited at different wavelengths in

the spectrum for the air side and the active layer side due to the difference in index of refraction (n = 1 for air and 1.47 for active layer material). The slope of the dispersion curve gives the speed of the wave along the interface, which depends on the dielectric functions of the metal and dielectric. A negative slope indicates the plasmon is travelling in the opposite direction along the surface. When $k_x = 0$, we expect surface plasmons to occur near $\pm mG$, where mG is defined in Eq. 29. For the active layer side of the grating, mG is modified by the index of refraction of the active layer. Lines indicating the Rayleigh anomalies are also drawn to help identify the surface plasmon order. Rayleigh anomalies occur when a diffraction order becomes evanescent and propagating waves travel along the interface of the two media.

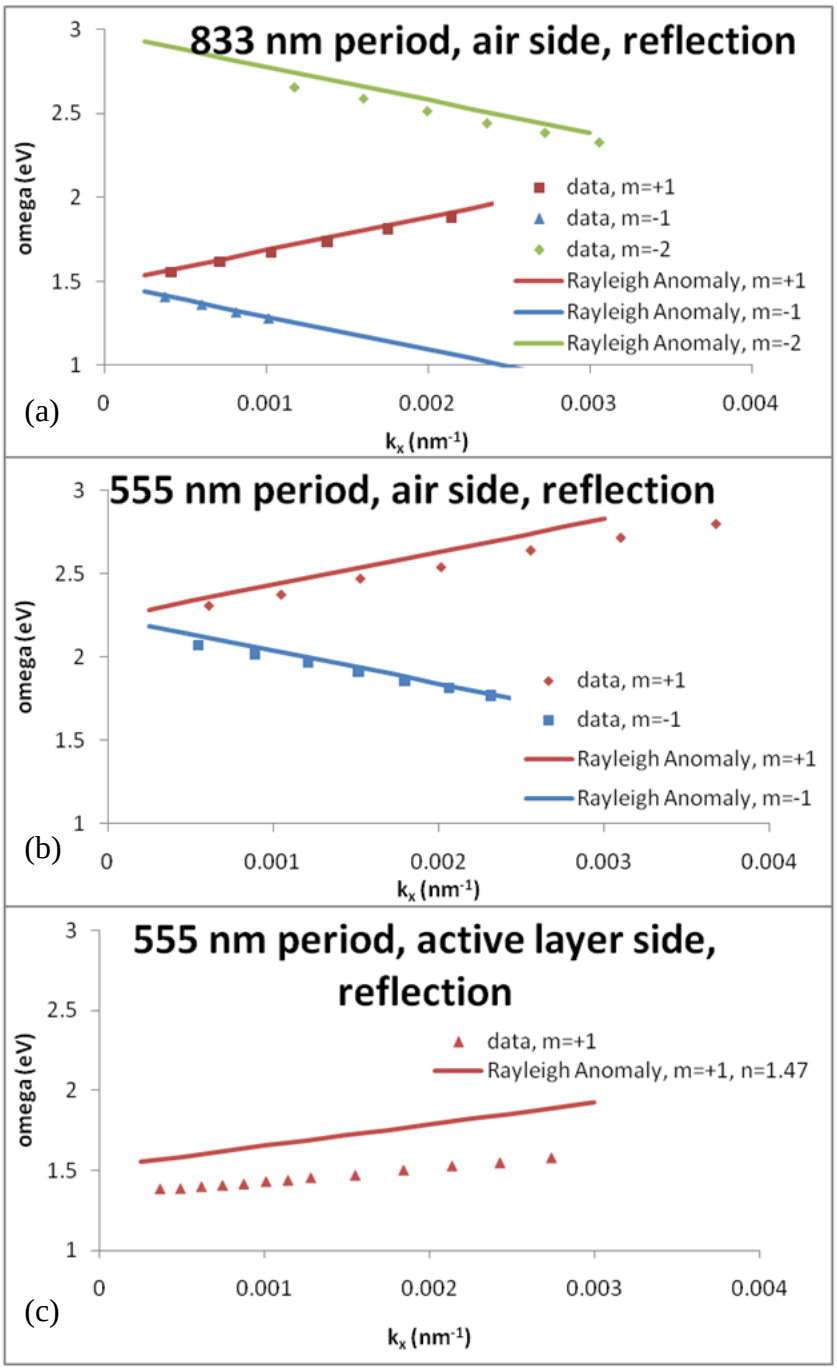

Figure 15: Dispersion curve for (a) an 833 nm patterned sample on the air side, (b) a 555 nm patterned sample on the air side, and (c) a 555 nm patterned sample on the active layer side.

It was possible to obtain transmission data because only 40 nm of Al was deposited on the sample. Transmission data were taken from θ = 0° to ~20°, as seen in Figure 16 (a-b), with the incident beam striking the active layer. For the 833 nm sample, the signal intensity of the

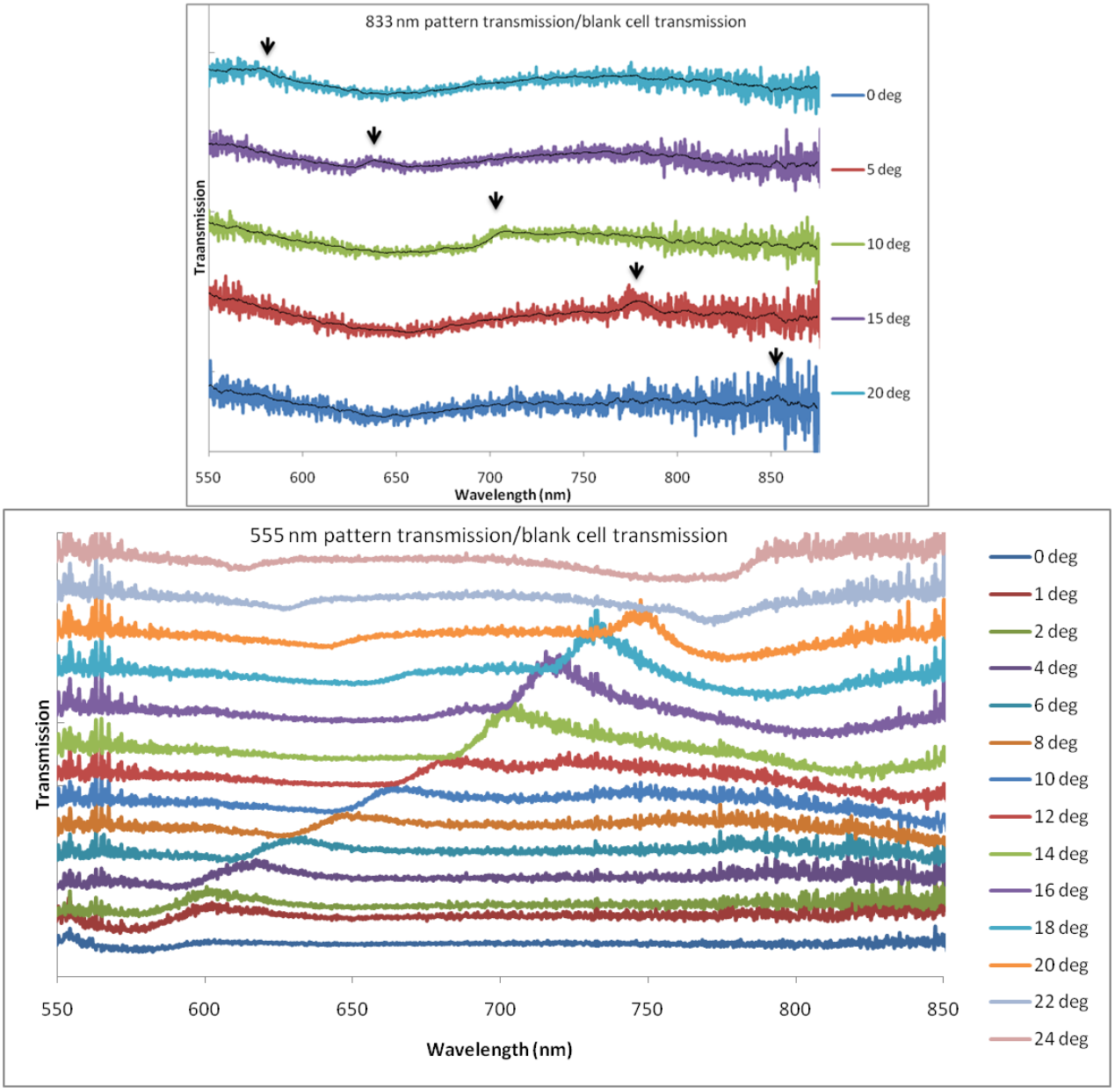

Figure 16: Transmission spectra of (a) 833 nm period cells and (b) 555 nm period cells.

transmission spectra was low; a moving average is used to help guide the eye. In Figure 17 (a-b) we see the corresponding dispersion curves.

Instead of the desired dips in transmission where we would expect higher absorption due to surface plasmons, we see peaks in transmission for the 833 nm patterned sample where the surface plasmon should be. Perhaps this can be explained by the thinness of the Al film and the reversibility of light coupling to a surface plasmon. Incoming light couples to a surface plasmon from the active layer side. Since the Al film is so thin, a surface plasmon is able to couple to the air side surface plasmon on the other side of the Al film. Because of reversibility, surface plasmons can then decouple from the film into light. In this scenario, we would expect peaks in transmission where surface plasmons decouple at the air interface, which is at the same

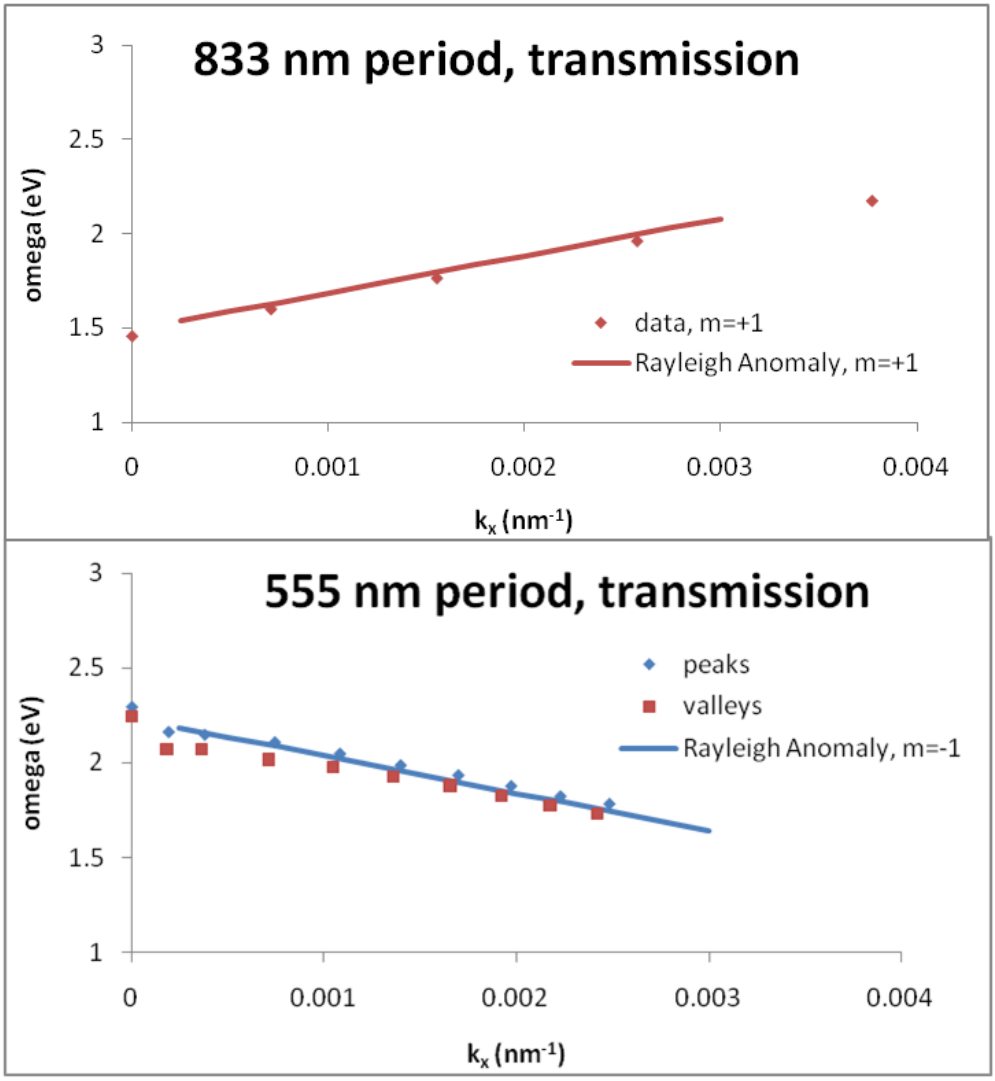

Figure 17: Dispersion curves for the transmission data of (a) 833 nm period grating cells and (b) 555 nm period cells. The Rayleigh anomaly is plotted with the data for respective orders of diffraction.

locations as dips in our reflection where surface plasmons couple at the air interface. Comparing our transmission dispersion curve in Figure 17 (a) to our reflection dispersion curve in Figure 15 (a), we see a very close correspondence between the transmission and reflection data, meaning we may have surface plasmon decoupling on the air/Al boundary.

The peaks in the transmission spectra for the 555 nm sample in Figure 16 (b) correspond to the Rayleigh Anomaly as seen in the dispersion curve, and the valleys appear on the dispersion curve where the surface plasmons should be. Because light interaction with such a thin film can be very complex and because we do not want any decoupling of light, thicker films (~125 nm) should be deposited in the future.

Surface plasmon measurements were also done with OPV samples dated from Spring 2009. The main difference in the two data sets is that the 2009 samples had an Al thickness of 125 nm, compared to the 2010 samples which had an Al thickness of 40 nm. These thicker gratings are opaque, guaranteeing that no light can be transmitted through the Al film and thus no surface plasmons can decouple from the air interface after coupling to the active layer interface. In Figure 18 we see surface plasmon dispersion curves from the thick Al samples (the raw data are in Appendix A: Reflection spectra of 2009 OPV cells). The data with thick Al films correspond well to the data taken from the March 2010 samples within the wavevector ranges where data were taken. Because we see surface plasmon coupling in the thicker films, and there is no decoupling, we can reasonably say that the light coupled to surface plasmons is being absorbed in the film.

Future work in this area will include measuring the surface plasmon resonances of OPV cells with silver electrodes. Because exposure to moisture and oxygen degrades our OPV cells, we were unable to take the cells out of the glove box in Austin until all IPCE measurements have been conducted on the cells. Once the measurements are complete, the cells will be brought back to San Antonio for surface plasmon reflection measurements.

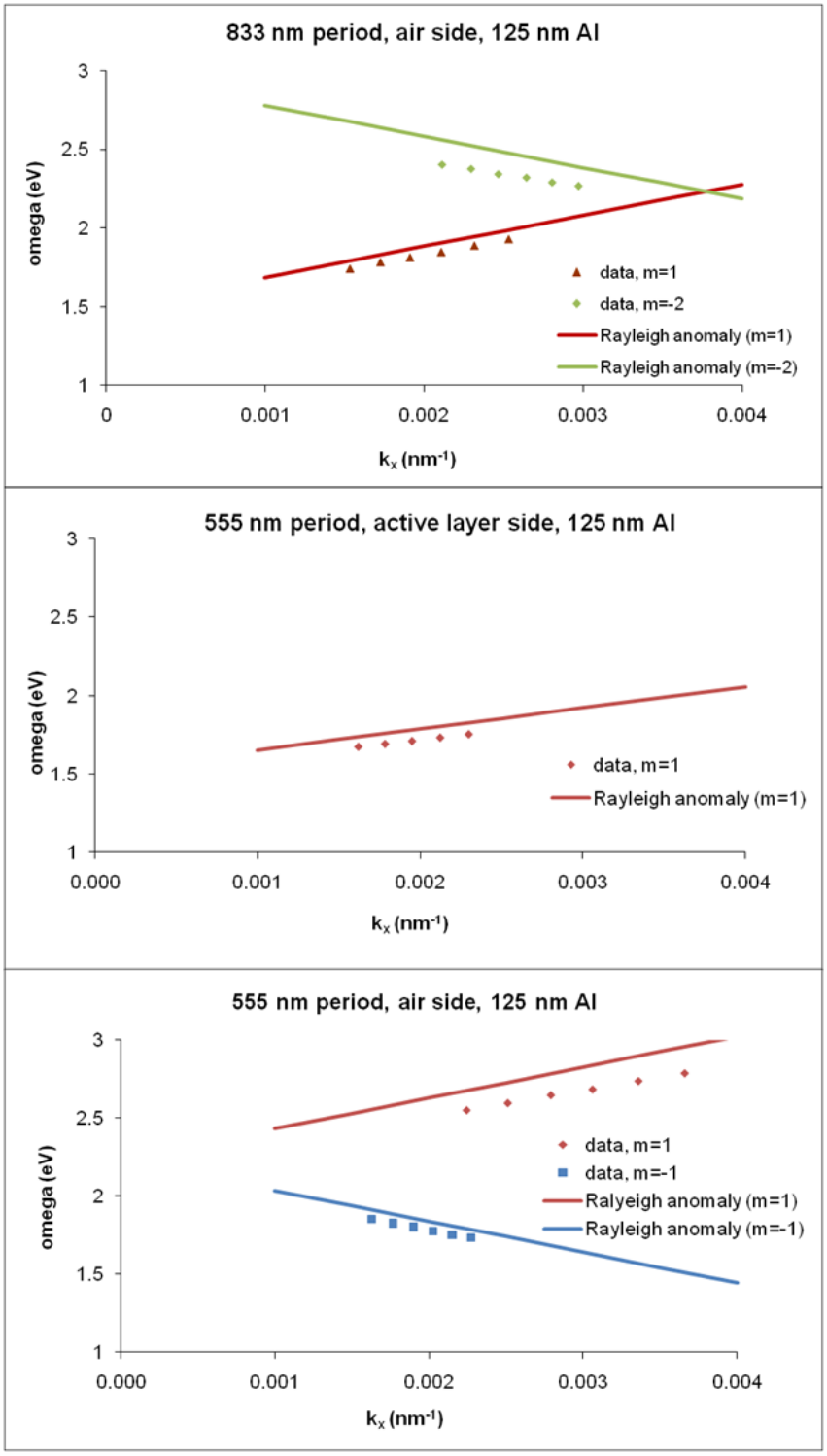

Figure 18: Dispersion curves with Al thickness of 125 nm for (a) 833 nm period grating cells, air side, (b) 555 nm period cells, air side, and (c) 555 nm period cells, active layer side. The Rayleigh anomaly is plotted with the data for respective orders of diffraction.

B. OPV Cell Efficiency Measurements

OPV cell open circuit voltage, short circuit current, and fill factor were measured from IV curves for solar cells made on April 1, 2010. Half the samples had Al cathodes and half had Ag cathodes. Unfortunately, the thickness of the cathodes is unknown in this set of devices because of problems with the thermal evaporator. Table 1 and Table 2 contain the average values and the gain values (patterned/unpatterned) for the Al cathode and Ag cathode cells respectively.

The IV curves of three typical devices are shown in Figure 19. Each device has a patterned and blank area, allowing for comparison of two cells within one device. It is important to note that our maximum cell efficiency is 1.2%, which is found in an unpatterned Al-cathode OPV cell. Although this may seem low, it is remarkably high considering that our chemicals are exposed to moisture and oxygen during the mixing and spin coating process.

Table 1: Average IV curve values for the Al samples.

ALUMINUM	**Voc (V)**	**Jsc (mA/cm^2)**	**FF**	**PCE (%)**
blank	0.8 ± 0.2	-5.1 ± 0.7	0.26 ± 0.02	1.0 ± 0.1
555 nm	1.02	-2.32	0.24	0.56
833 nm	0.6 ± 0.1	-5.1 ± 0.2	0.26 ± 0.01	0.83 ± 0.2
	Voc gain	**Jsc gain**	**FF gain**	**PCE gain**
555 gain	1.30	0.46	0.91	0.56
833 gain	0.8 ± 0.4	1.0 ± 0.2	1.0 ± 0.1	0.8 ± 0.3

Table 2: Average IV curve values for the Ag samples.

SILVER	**Voc (V)**	**Jsc (mA/cm^2)**	**FF**	**PCE (%)**
blank	0.34 ± 0.03	-2.0 ± 0.3	0.32 ± 0.01	0.28 ± 0.04
555 nm	0.4 ± 0.1	-2.5 ± 0.2	0.34 ± 0.03	0.32 ± 0.05
833 nm	0.39 ± 0.07	-2.8 ± 0.6	0.32 ± 0.01	0.33± 0.01
	Voc gain	**Jsc gain**	**FF gain**	**PCE gain**
555 gain	1.0 ± 0.4	1.1 ± 0.2	1.0 ± 0.1	1.1 ± 0.3
833 gain	1.1 ± 0.3	1.2 ± 0.4	1.00 ± 0.01	1.2 ± 0.2

As of yet, no significant gain in fill factor or efficiency was seen for patterned cells versus blank cells. This could be due to large error caused by few data points, and high irregularities from device to device. Although we fabricated 14 devices with 28 OPV cells in one run, 12 of those OPV cells were shorted or passed no current, leaving us with 16 functioning OPV cells for testing. In particular, only one of the 555 nm patterned aluminum cathode cells was not shorted, so no error analysis was performed for that set. Since small sample sizes give very large standard deviations, standard deviation might not be the best way for us to calculate error. It is encouraging that in the silver

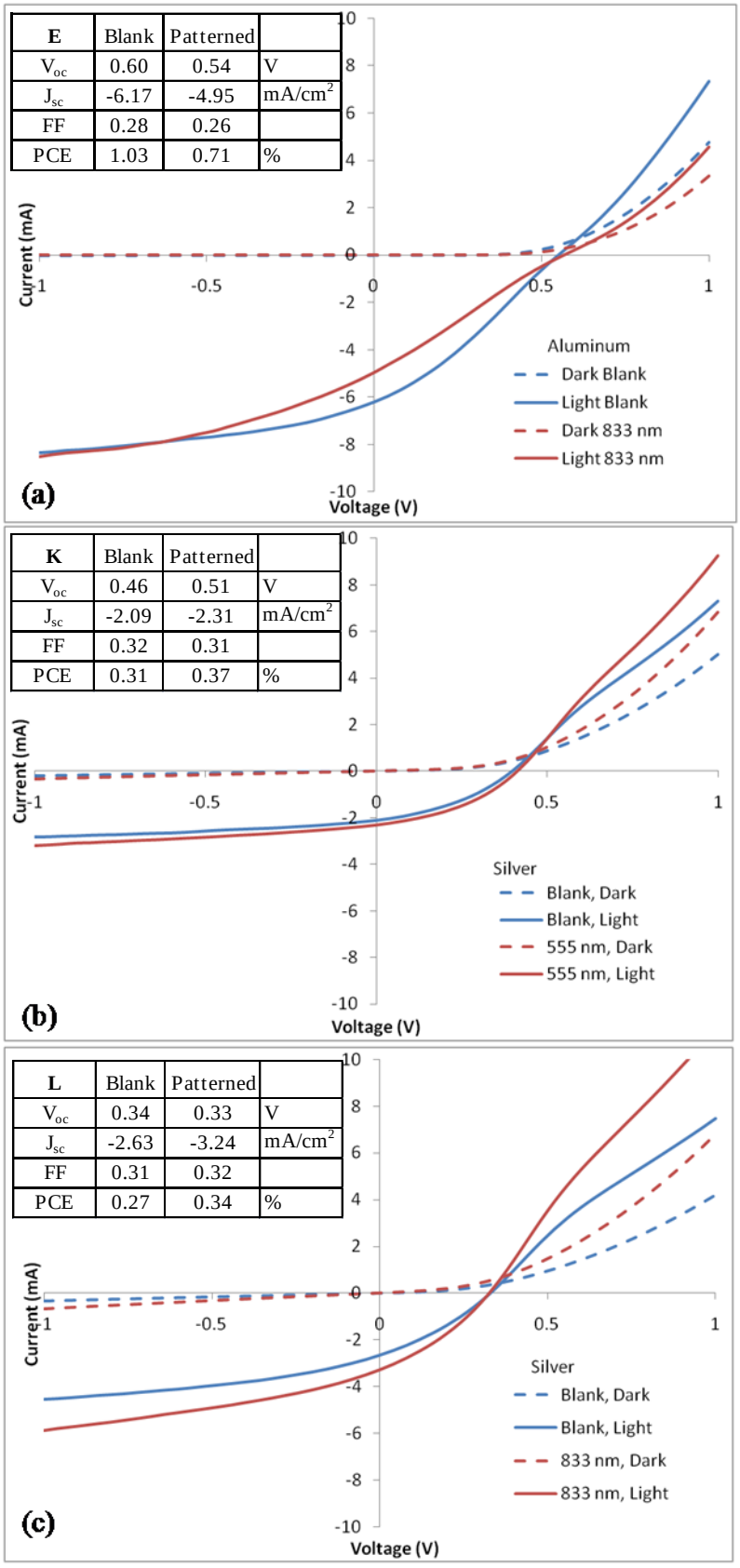

Figure 19: IV curves for (a) an Al cathode cell with an 833 nm grating, (b) a Ag cathode cell with a 555 nm grating, and (c) a Ag cell with an 833 nm grating.

samples, in which we only had 3 out of 14 cells short, we see gain values greater than or equal to one. Thus, we hope with less device inconsistency, our error will be reduced enough to give us significant results.

If we were to increase the absorption efficiency of the OPV cell, we would expect to see the short circuit current density increase, causing an increase in fill factor and efficiency. The reason we expect the current to increase is because as the device absorbs more photons, more electron-hole pairs will be created and more current will flow. Our largest gain parameters are in the short circuit current density. If this is found later to be a statistically significant gain, then our hypothesis that we are increasing the absorption efficiency would be supported.

IPCE curves, which correspond to measuring the efficiency of the OPV cells as a function of wavelength, were measured for devices made on March 10, 2010 and April 1, 2010. In Figure 20, curves for typical devices from March 10, 2010 are plotted. In Figure 20, typical devices from March 10, 2010 are plotted. We can see that our OPV devices generate power in the 330 to 700 nm wavelength range, or roughly the visible spectrum, with the upper limit corresponding to the HOMO/LUMO gap of the active layer.

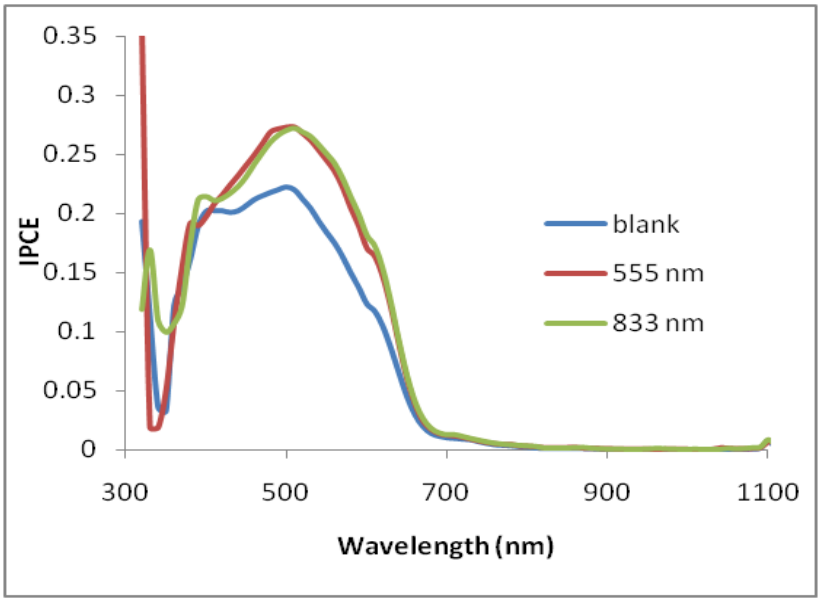

Figure 20: IPCE for a blank, 555 nm grating, and 833 nm grating OPV cell, March 10, 2010.

The IPCE for the OPV devices from April 1, 2010 is shown in Figure 21 from 400 to 900 nm in 2 nm increments with their corresponding gain curves. Again, this set of devices allows direct comparison between blank and patterned OPV cells on the same device. We have IPCE curves for sample E, which has an Al cathode for an 833 nm cell and a blank cell, as seen in Figure 21 (a). The peak IPCE for both cells is over 0.50 at 480 nm. The silver samples are shown in Figure 21 (b and c), for 555 nm and 833 nm periods, respectively. The maximum IPCE for

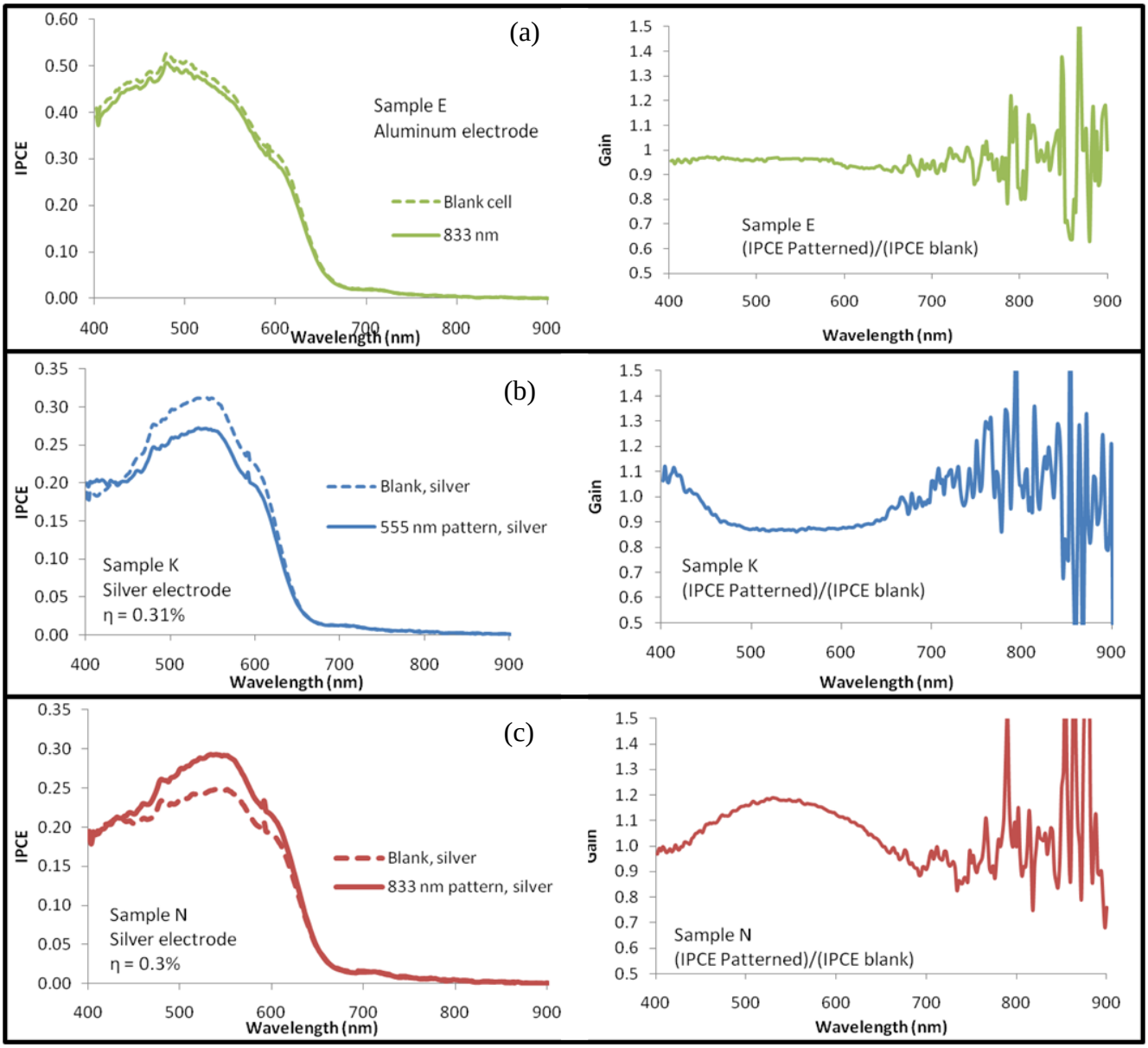

Figure 21: IPCE for patterned and blank samples and the gain. Shown for (a) Al sample with 833 nm period, (b) Ag sample with 555 nm period, and (c) Ag sample with 833 nm period, April 1, 2010.

sample K, the silver sample with a 555 nm pattern, is 0.30 at 534 nm for the blank side and 0.26 at 544 nm for the patterned side. The maximum IPCE for sample N, the silver sample with a 833 nm pattern, is 0.25 at 536 nm for the blank side and 0.29 at 532 nm for the patterned side.

We do not see a gain in IPCE for the selected patterned devices over the blank devices over all of the cells. We do see an overall gain in Sample N, which peaks at 526 nm. While this does not correspond to a surface plasmon order, this may be due to overall enhancement of absorption due to the increased optical path in the active layer of the first diffraction order as it is still propagating for the visible wavelengths. However, this conclusion is uncertain because we do not see this increase across all devices. The magnitude change in IPCE may instead be attributed to device inconsistency – because of the geometry of our devices and our spin coating methods, the patterned part of the device had a thinner active layer than the blank part.

An interesting feature in our IPCE graphs of one of the 555 nm and one of the 833 nm silver OPV devices, samples K and L, is the higher patterned device IPCE from ~ 400 to 450 nm, even though we have lower patterned device IPCE at higher wavelengths, seen in Figure 22. For the 555 nm device, this corresponds with a second order surface plasmon on the active layer side at 416 nm, and for the 833 nm device, this corresponds to a third order surface plasmon on the active layer side at 416 nm. The IPCE curve of sample K

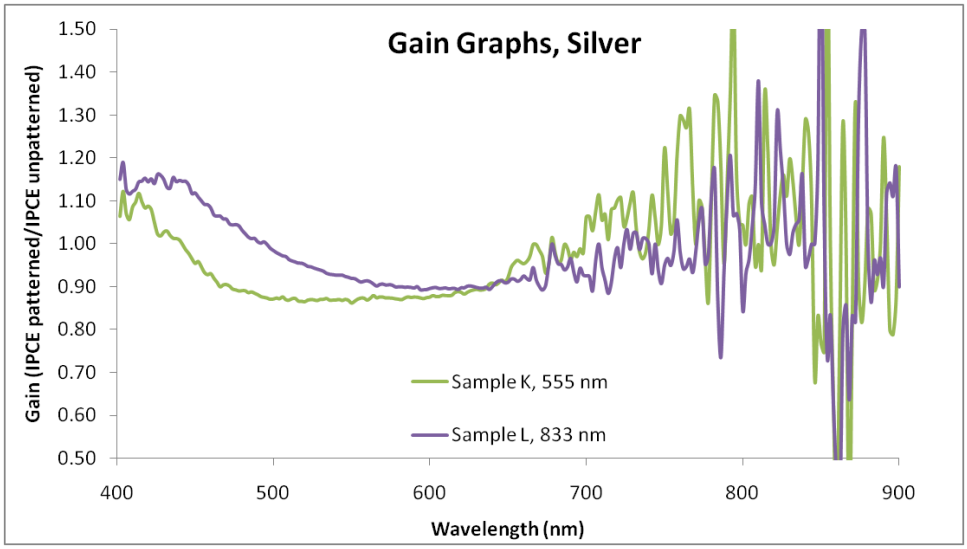

Figure 22: Gain graphs of 555 nm and 833 nm silver samples.

is shown in Figure 21 (b) and the IPCE curve of sample L is shown in Figure 23.

In order to determine if these peaks are due to surface plasmon resonance, data should be taken to lower wavelengths and the IPCE should be measured at different incidence angles. Because of temporary technical difficulties with the glove box in which these measurements are made, we were unable to get angle-resolved measurements on our last trip to Austin.

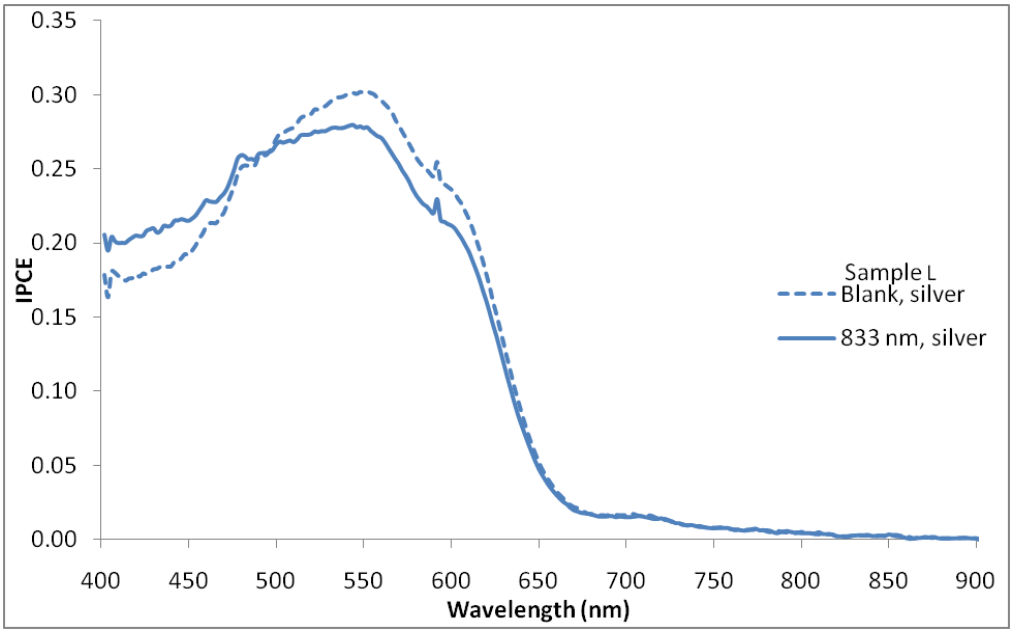

Figure 23: IPCE curve for Sample L, with an 833 nm patterned cathode.

V. Conclusions

OPV cells have recently attracted attention due to their low cost and easy fabrication. However, efficiency remains low compared to silicon-based photovoltaics. One reason for their low efficiency is that the requirement for a thin active layer leads to low light absorption. This thesis investigated using surface plasmons to boost absorption by patterning the bottom Ag or Al electrode with either a 555 nm or 833 nm period grating. Surface plasmons were verified to exist on Al cathode cells by reflection and transmission measurements. Silver cathode cells were not measured because they are still in the glove box in Austin awaiting further IPCE measurements. Although we could not say within error that efficiency, fill factor, V_{OC}, or J_{SC} increased or decreased for our patterned versus unpatterned OPV cells, this could be due to the large error that results from having only a few functioning samples. While there was no overall gain in IPCE for the samples with gratings to couple surface plasmons, silver cathode samples showed potential gains in IPCE due to surface plasmons around 400 to 450 nm for both 555 nm and 833 nm period gratings. Further experiments are necessary to fully investigate the role of the surface plasmon in this increase in efficiency.

VI. References

1. Sam-Shajing Sun and Niyazi Serdar Sariciftci, in Organic Photovoltaics: Mechanisms, Materials, and Devices, edited by Sam-Shajing Sun and Niyazi Serdar Sariciftci (CRC Press, Boca Raton, FL, 2005), Preface.

2. Martin A. Green, Keith Emery, Yoshihiro Hishikawa and Wilhelm Warta, Prog. Photovolt: Res. Appl. 17, 320 (2009).

3. UNSW, School of Photovoltaic and Renewable Energy Engineering, *Third Generation Photovoltaics*, http://www.pv.unsw.edu.au/Research/3gp.asp (2010).

4. Harry A. Atwater and Albert Polman, Nat. Mater. 9, 205 (2010).

5. Martin A. Green, Solar Cells: Operating Principles, Technology and System Applications, (The University of New South Wales, Kensington, NSW, Australia, 1998), p. 274.

6. Rieke Metals, Inc. "Product Catalog." <http://riekemetals.thomasnet.com/item/cialty-conducting-polymers-product-numbers-4000-s-/poly-3-hexylthiophene-2-5-diyl-p3ht/4002-e-2?&seo=1>.

7. Wray, Lisa. "Nano-C: nanostructured carbon materials that power our world." 2008. <http://www.nano-c.com/fullerenederivatives.html>.

8. Steffi Sensfuss and Maher Al-Ibrahim, in Organic Photovoltaics: Mechanisms, Materials, and Devices, edited by Sam-Shajing Sun and Niyazi Serdar Sariciftci (CRC Press, Boca Raton, FL, 2005), Chap. 23, pp. 529.

9. Brian A. Gregg, in Organic Photovoltaics: Mechanisms, Materials, and Devices, edited by Sam-Shajing Sun and Niyazi Serdar Sariciftci (CRC Press, Boca Raton, FL, 2005), Chap. 6, pp. 139.

10. Alex C. Mayer, Shawn R. Scully, Brian E. Hardin, Michael W. Rowell and Michael D. McGehee, Mater. Today 10, 28 (2007).

11. Aleksandra B. Djurisic and Chung Yin Kwong, in Organic Photovoltaics: Mechanisms, Materials, and Devices, edited by Sam-Shajing Sun and Niyazi Serdar Sariciftci (CRC Press, Boca Raton, FL, 2005), Chap. 20, pp. 453.

12. Paul A. Lane and Zakya H. Kafafi, in Organic Photovoltaics: mechanisms, materials, and devices, edited by Sam-Shajing Sun and Niyazi Serdar Sariciftci (CRC Press, Boca Raton, FL, 2005), Chap. 4, pp. 49-63.

13. Harald Hoppe and Niyazi Serdar Sariciftci, in Organic Photovoltaics: Mechanisms, Materials, and Devices, edited by Sam-Shajing Sun and Niyazi Serdar Sariciftci (CRC Press, Boca Raton, FL, 2005), Chap. 9, pp. 217.

14. Seok-In Na, Deok-Soon Kim, Soon-Shin Kwon, Jang Jo, Juhwan Kim, Takhee Lee and Dong-Yu Kim, APL 91, (2007).

15. Keisuke Nakayama, Katsuaki Tanabe and Harry A. Atwater, App. Phys. Lett. 93, 121904 (2008).

16. Lucimara Stolz Roman, Olle Inganas, Thomas Granlund, Tobias Nyberg, Mattias Svensson, Mats R. Anderson and Jan C. Hummelen, Adv. Mat. 12, 189 (2000).

17. Nathan C. Lindquist, Wade A. Luhman, Sang-Hyun Oh and Russell J. Holmes, App. Phys. Lett. 93, 123308 (2008).

18. Heinz Raether, Surface Plasmons on Smooth and Rough Surfaces and on Gratings, (Springer-Verlag, Berlin, Germany, 1988), p. 136.

19. P. B. Johnson and R. W. Christy, Phys. Rev. B 6, 4370 (1972).

20. D. Y. Smith, E. Shiles and Mitio Inokuti, in Handbook of Optical Constants and Solids, edited by Edward D. Palik (Academic Press, Inc., Orlando, 1985), pp. 369.

21. Seok-In Na, Seok-Soon Kim, Jang Jo, Seung-Hwan Oh, Juhwan Kim and Dong-Yu Kim, Adv. Funct. Mater. 18, 3956 (2008).

22. Organic Solar Cells / OSC application guide." Clevios: The Ultimate Conductive Polymer. 2005. H.C. Stark. 11 May 2009 <http://www.clevios.com/index.php?page_id=3014>.

23. Fengling Zhang and Olle Inganas, in Organic Photovoltaics: Mechanisms, Materials, and Devices, edited by Sam-Shajing Sun and Niyazi Serdar Sariciftci (CRC Press, Boca Raton, FL, 2005), Chap. 21, pp. 479.

24. Stefan A. Maier and Harry A. Atwater, J. of App. Phys 98, 011101 (2005).

VII. Appendix A: Reflection spectra of 2009 OPV cells.

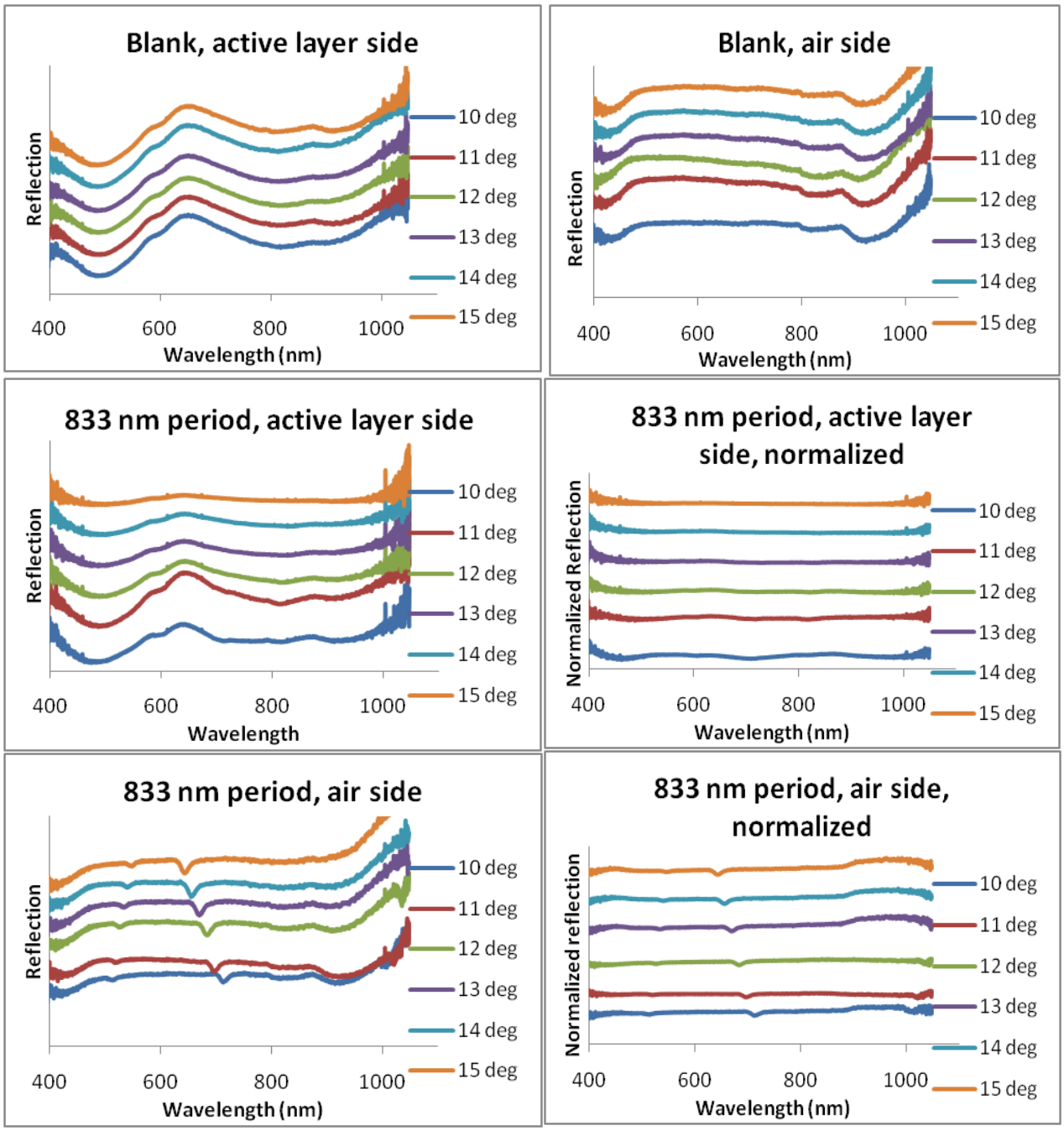

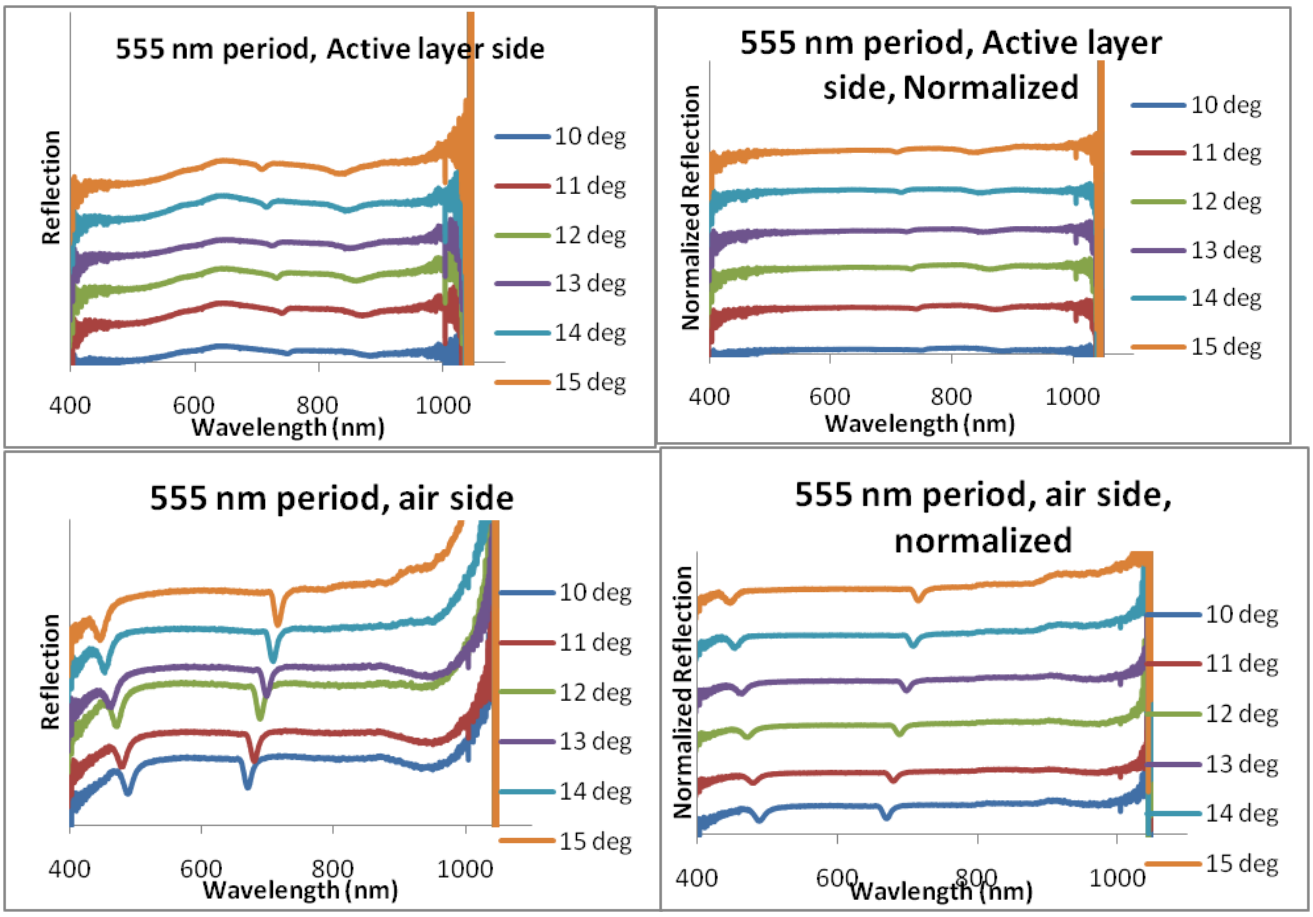
555 nm period, Active layer side
Reflection
Wavelength (nm)
400
600
800
1000
10 deg
11 deg
12 deg
13 deg
14 deg
15 deg
555 nm period, Active layer side, Normalized
Normalized Reflection
Wavelength (nm)
555 nm period, air side
Reflection
Wavelength (nm)
555 nm period, air side, normalized
Normalized Reflection
Wavlength (nm)